

# A first glimpse at the influence of body mass in the morphological integration of the limb long bones: an investigation in modern rhinoceroses

Christophe Mallet<sup>1</sup>  | Guillaume Billet<sup>2</sup>  | Alexandra Houssaye<sup>1</sup>  |  
Raphaël Cornette<sup>3</sup> 

<sup>1</sup>Mécanismes adaptatifs et évolution (MECADEV), UMR 7179, MNHN, CNRS, Paris, France

<sup>2</sup>Centre de Recherche en Paléontologie – Paris (CR2P), UMR CNRS 7207, MNHN, CNRS, France

<sup>3</sup>Institut de Systématique, Evolution, Biodiversité (ISYEB), UMR 7205, MNHN, CNRS, SU, EPHE, UA, Paris, France

## Correspondence

Christophe Mallet, Mécanismes adaptatifs et évolution (MECADEV), UMR 7179, MNHN, CNRS, 55 rue Buffon, CP 55, 75005, Paris, France.

Email: christophe.mallet@edu.mnhn.fr

## Funding information

H2020 European Research Council, Grant/Award Number: ERC-2016-STG-715300

## Abstract

The appendicular skeleton of tetrapods is a particularly integrated structure due to the shared developmental origin or similar functional constraints exerted on its elements. Among these constraints, body mass is considered strongly to influence its integration but its effect on shape covariation has rarely been addressed in mammals, especially in heavy taxa. Here, we propose to explore the covariation patterns of the long bones in heavy animals and their link to body mass. We investigate the five modern rhinoceros species, which display an important range of bodyweight. We used a 3D geometric morphometric approach to describe the shape covariation of the six bones composing the stylopodium and zeugopodium both among and within species. Our results indicate that the appendicular skeleton of modern rhinos is a strongly integrated structure. At the interspecific level, the shape covariation is roughly similar between all pairs of bones and mainly concerns the muscular insertions related to powerful flexion and extension movements. The forelimb integration appears higher and more related to body mass than that of the hind limb, suggesting a specialization for weight support. The integration of the stylopodium elements does not seem to relate to body mass in our sample, which suggests a greater effect of shared developmental factors. Conversely, the covariation of the zeugopodium bones seems more associated with body mass, particularly for the radius-ulna pair. The fibula appears poorly integrated with other bones, especially within non-*Rhinoceros* species, which may represent a case of parcellation due to a functional dissociation between the hind limb bones. The exploration of the integration patterns at the intraspecific level also highlights a more prominent effect of age over individual body mass on shape covariation within *C. simum*. This study lends support to previous hypotheses indicating a link between high body mass and high integration level.

## KEYWORDS

appendicular skeleton, body mass, functional morphology, geometric morphometrics, locomotion, morphological integration, Rhinocerotidae

1 | INTRODUCTION

The morphology of the different anatomical parts constituting organisms is known to be influenced by interactions between these parts due to shared developmental origin, phylogenetic legacy, functional constraints or structural requirements (Olson and Miller, 1958; Van Valen, 1965; Cheverud, 1982; Gould, 2002; Hallgrímsson *et al.*, 2002; Cubo, 2004; Goswami and Polly, 2010; Goswami *et al.*, 2014). The tendency of morphological traits to covary under the influence of these factors is known as morphological integration (Olson and Miller, 1958; Van Valen, 1965). These factors can increase morphological integration of the whole body or parts of it, but they can also act locally to produce stronger covariation within parts than with other units (e.g. modules—Hallgrímsson *et al.*, 2002; Young and Hallgrímsson, 2005; Klingenberg, 2008; Goswami *et al.*, 2014). Morphological integration is therefore classically explored through the study of covariation between sets of linear measurements or shape data (Van Valen, 1965; Klingenberg, 2008; Goswami and Polly, 2010; Bookstein, 2015).

Among tetrapods, the appendicular skeleton is a particularly integrated structure due to the common developmental origin of its parts (serial homology—Young and Hallgrímsson, 2005; Bininda-Emonds *et al.*, 2007; Sears *et al.*, 2015) and shared functional constraints linked to locomotion and ecology (Hallgrímsson *et al.*, 2002; Young and Hallgrímsson, 2005; Goswami *et al.*, 2014; Martín-Serra *et al.*, 2015; Botton-Divet *et al.*, 2018). In this framework, it has been hypothesized that the functional specialization of the appendicular skeleton is associated with a decrease of the integration level between limbs and serially homologous elements, and an increase of the within-limb integration (Hallgrímsson *et al.*, 2002; Young and Hallgrímsson, 2005). This has been particularly observed for some extreme locomotor adaptations such as flight in bats or bipedal locomotion in hominoids, which led to a strong specialization of a specific part of the appendicular skeleton and consequently to a decrease of

the general integration (Young and Hallgrímsson, 2005; Young *et al.*, 2010; Bell *et al.*, 2011). Moreover, among quadrupedal mammals, the loss of the clavicle allows a greater mobility of the scapula, playing an active role in locomotion (Gasc, 2001; Schmidt and Fischer, 2009). This led to a shift in the functional relations between limb parts, where the serially homologous elements are not functionally analogous anymore (Gasc, 2001; Schmidt and Fischer, 2009) (Figure 1). At the interspecific level (e.g. evolutionary integration—Klingenberg, 2014), it has been shown that many terrestrial taxa (equids, carnivorans, marsupials) present a strong general integration among all their limb long bones (Bennett and Goswami, 2011; Kelly and Sears, 2011; Fabre *et al.*, 2014; Martín-Serra *et al.*, 2015; Hanot *et al.*, 2017; 2018; 2019; Botton-Divet *et al.*, 2018; Martín-Serra and Benson, 2019), with a covariation mainly linked to the locomotion and shared phylogenetic history. But few studies have explored the patterns of morphological integration of the appendicular skeleton among mammals at the intraspecific level (e.g. static or developmental integration—Klingenberg, 2014) and attempted to compare them with the patterns observed at the interspecific level (Young *et al.*, 2010; Hanot *et al.*, 2017; 2018; 2019).

The support of a heavy mass is likely an important factor influencing the shape and integration of the appendicular skeleton. Among mammals, many lineages displayed an increase of their body mass along their evolutionary history (Depéret, 1907; Raia *et al.*, 2012; Baker *et al.*, 2015; Bokma *et al.*, 2016). Biomechanical studies indicate that the shape of the limb bones should be driven by stress linked to mass support during the stance and the displacement of the animal (Hildebrand, 1974; Biewener, 1983; 1989a; 1989b). However, few studies have explored the precise role exerted by body mass on the shape variation of the limb bones (Biewener, 1983; Bertram and Biewener, 1992; Fabre *et al.*, 2013; Mallet *et al.*, 2019). Likewise, the influence of body mass on integration patterns among limb bones is poorly known. Previous studies on relatively light taxa have indicated a limited effect of body mass on integration patterns, overcome

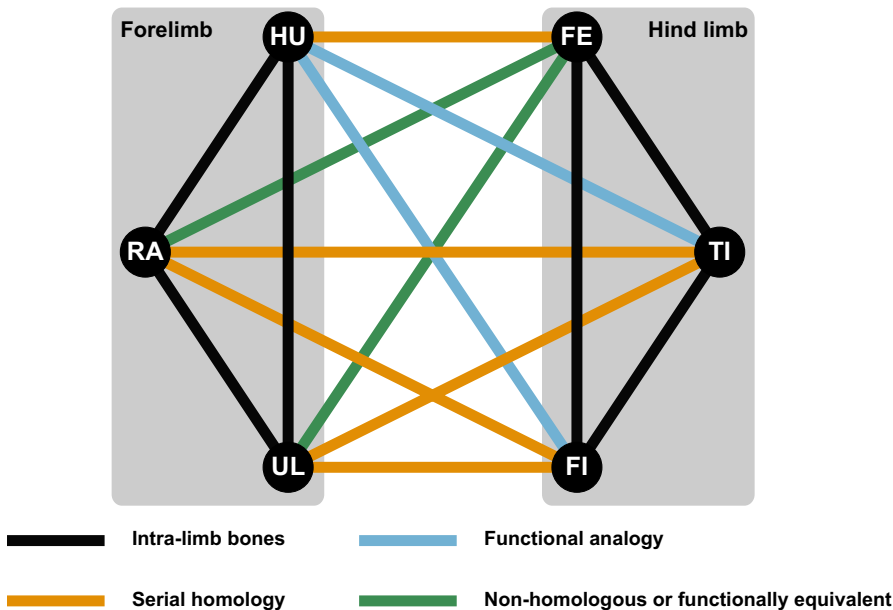


**FIGURE 1** Figure Graphic model showing the hypotheses of morphological integration tested in this study on the appendicular skeleton of the five modern rhino species. HU: humerus; RA: radius; UL: ulna; FE: femur; TI: tibia; FI: fibula

by other factors such as locomotor ecology (Martín-Serra *et al.*, 2015; Botton-Divet *et al.*, 2018; Martín-Serra and Benson, 2019). Conversely, other works have proposed that body mass may still have an impact on the shape covariation of the limb long bones (Hanot *et al.*, 2017; Randau and Goswami, 2018), possibly more pronounced for heavier species (Schmidt and Fischer, 2009). Drawing on this, we chose to explore the integration patterns among modern rhinoceroses, which constitute the second heaviest terrestrial group after elephants among modern mammals (Alexander and Pond, 1992). Whereas body size and mass poorly vary among the three species of elephants, the five modern species of rhinos surviving today display a wide range of body mass (BM): *Dicerorhinus sumatrensis* (Fischer, 1814)—mean body mass (BM): 775 kg; *Diceros bicornis* (Linnaeus, 1758)—mean BM: 1,050 kg; *Rhinoceros sondaicus* Desmarest, 1822—mean BM: 1,350 kg; *Rhinoceros unicornis* Linnaeus, 1758—mean BM: 2,000 kg; *Ceratotherium simum* (Burchell, 1817)—mean BM: 2,300 kg (Dinerstein, 2011). This range of body mass can be highly variable within each species due to sexual dimorphism or between wild and captive specimens: 600–950 kg for *Ds. sumatrensis*; 800–1,300 kg for *Dc. bicornis*; 1,200 – 1,500 kg for *R. sondaicus*; 1,270–2,800 kg for *R. unicornis*; 1,350–3,500 kg for *C. simum* (Zschokke and Baur, 2002; Dinerstein, 2011). *Ceratotherium simum* and *Dc. bicornis* are present in Africa, while the three other species live only in Asia. While a few studies have explored the shape variation of their long bones in relation to the ecology, phylogeny and functional constraints, such as body mass (Guérin, 1980; Eisenmann and Guérin, 1984; Mallet *et al.*, 2019), no work has focused on the integration of their appendicular skeleton and its relationship to these factors. The aim of this study is thus to explore shape covariation patterns among limb long bones within and between species in order to highlight the potential influence of body mass.

Here, we propose to investigate the integration patterns of the shape of the limb long bones among the five species of modern rhinos, to quantify the integration level within and between limbs and to explore whether body mass could influence covariation patterns. To describe precisely the shape covariations by taking into consideration the whole shape of the bones in three dimensions, our analyses were done using 3D geometric morphometrics. They were performed at both interspecific and intraspecific levels, taking phylogenetic relationships into account where necessary. Although phylogeny is still debated among rhinos, notably regarding the position of *Ds. sumatrensis*, the monophyly of the African rhinos (*Ceratotherium* and *Diceros*) and of *Rhinoceros* species is considered consensual (Gaudry, 2017; Antoine, 2002; Willerslev *et al.*, 2009; Cappellini *et al.*, 2019). In accordance with previous works, we hypothesize that the shape of limb long bones among rhinos should be: (a) strongly integrated as in other quadrupedal mammals at both interspecific and intraspecific levels (Hanot *et al.*, 2017); (b) relatively homogeneous between fore- and hind limbs, as in other quadrupedal mammals (Martín-Serra *et al.*, 2015; Hanot *et al.*, 2017); (c) more strongly integrated than in lighter mammal species (Schmidt and Fischer, 2009); and (d) show similar patterns of shape covariation at both interspecific and intraspecific levels (Klingenberg, 2014). This will allow us to highlight how body

mass could influence the structure of the limb long bones among rhinos.

## 2 | METHODS

### 2.1 | Studied sample

The dataset was composed of 50 complete skeletons housed in different European and American museums and belonging to the five extant rhino species: *Ceratotherium simum* (15 specimens), *Dicerorhinus sumatrensis* (9 specimens), *Diceros bicornis* (10 specimens), *Rhinoceros sondaicus* (7 specimens) and *Rhinoceros unicornis* (9 specimens) (Table 1). We considered individuals with fully fused epiphyses (adults) or individuals where the line of the epiphyseal plates was still visible on some bones (subadults). Bones with breakages or unnatural deformations were not selected. The sample involved males, females and specimens without sex information, as well as captive and wild specimens. All anatomical terms follow classic anatomical and veterinary works (Guérin, 1980; Federative Committee on Anatomical Terminology, 1998; Antoine, 2002; Barone, 2010) and are given in Figure S1.

### 2.2 | 3D models

Most of the bones were digitized using a structured-light three-dimensional scanner (Artec Eva) and reconstructed with Artec Studio Professional software (v12.1.1.12—Artec 2018, 2018). Twelve bones were digitized with a photogrammetric approach, following Mallison and Wings (2014) and Fau, Cornette and Houssaye (2016). Sets of photos were used to reconstruct 3D models using Agisoft Photoscan software (v1.4.2—Agisoft, 2018). Each mesh was decimated to reach 250,000 vertices and 500,000 faces using MESHLAB software (v2016.12—Cignoni *et al.*, 2008). Only left bones were selected for digitization; when left sides were not available, right bones were selected instead and mirrored before analysis.

### 2.3 | 3D geometric morphometrics

The shape covariation was analysed using a 3D geometric morphometrics approach. This widely used methodology allows to quantify the morphological differences between objects by comparing the spatial coordinates of points called landmarks (Adams *et al.*, 2004; Zelditch *et al.*, 2012). This method can also be easily extended to the study of shape covariation (Goswami and Polly, 2010; Bardua *et al.*, 2019). Bone shape was quantified by placing a set of anatomical landmarks and curve and surface sliding semi-landmarks on the meshes, following Gunz and Mitteroecker (2013), Botton-Divet *et al.* (2016) and Mallet *et al.* (2019). We placed all landmarks and curves using the IDAV LANDMARK software (v3.0—Wiley *et al.*, 2005). We created a template to place surface semi-landmarks for each bone. We

**TABLE 1** List of the studied specimens with sex, age class, condition and 3D acquisition details

Taxon	Institution	Specimen number	Sex	Age	Condition	3D acquisition
<i>Ceratotherium simum</i>	AMNH	M-51854	F	A	W	SS
<i>Ceratotherium simum</i>	AMNH	M-51855	M	A	W	SS
<i>Ceratotherium simum</i>	AMNH	M-51857	F	A	W	SS
<i>Ceratotherium simum</i>	AMNH	M-51858	M	A	W	SS
<i>Ceratotherium simum</i>	AMNH	M-81815	U	A	U	SS
<i>Ceratotherium simum</i>	BICPC	NH.CON.20	M	S	W	SS
<i>Ceratotherium simum</i>	BICPC	NH.CON.32	F	S	W	SS
<i>Ceratotherium simum</i>	BICPC	NH.CON.40	F	S	W	SS
<i>Ceratotherium simum</i>	BICPC	NH.CON.110	M	A	W	SS
<i>Ceratotherium simum</i>	BICPC	NH.CON.112	M	A	W	SS
<i>Ceratotherium simum</i>	NHMUK	ZD 2018.143	U	A	U	SS
<i>Ceratotherium simum</i>	NHMW	3086	U	A	W	P
<i>Ceratotherium simum</i>	RBINS	19904	M	S	W	SS
<i>Ceratotherium simum</i>	RMCA	1985.32-M-0001	U	A	W	SS
<i>Ceratotherium simum</i>	RMCA	RG35146	M	A	W	SS
<i>Dicerorhinus sumatrensis</i>	MNHN	ZM-AC-1903-300	M	A	W	SS
<i>Dicerorhinus sumatrensis</i>	NHMUK	ZD 1879.6.14.2	M	A	W	SS
<i>Dicerorhinus sumatrensis</i>	NHMUK	ZD 1894.9.24.1	U	A	W	SS
<i>Dicerorhinus sumatrensis</i>	NHMUK	ZD 1931.5.28.1	M	S	W	SS
<i>Dicerorhinus sumatrensis</i>	NHMUK	ZE 1948.12.20.1	U	A	U	SS
<i>Dicerorhinus sumatrensis</i>	NHMUK	ZE 1949.1.11.1	U	A	W	SS
<i>Dicerorhinus sumatrensis</i>	NHMW	3082	U	A	U	P
<i>Dicerorhinus sumatrensis</i>	RBINS	1204	M	A	W	SS
<i>Dicerorhinus sumatrensis</i>	ZSM	1908/571	M	A	U	SS
<i>Diceros bicornis</i>	AMNH	M-81805	U	A	U	SS
<i>Diceros bicornis</i>	AMNH	M-27757	M	S	W	SS
<i>Diceros bicornis</i>	AMNH	M-113776	U	A	W	SS
<i>Diceros bicornis</i>	AMNH	M-113777	U	A	W	SS
<i>Diceros bicornis</i>	AMNH	M-113778	U	A	W	SS
<i>Diceros bicornis</i>	MNHN	ZM-AC-1936-644	F	S	U	SS
<i>Diceros bicornis</i>	RBINS	9714	F	A	W	SS
<i>Diceros bicornis</i>	RMCA	RG2133	M	S	W	SS
<i>Diceros bicornis</i>	ZSM	1961/186	M	S	U	SS
<i>Diceros bicornis</i>	ZSM	1961/187	M	S	U	SS
<i>Rhinoceros sondaicus</i>	CCEC	50002041	U	A	W	SS
<i>Rhinoceros sondaicus</i>	MNHN	ZM-AC-A7970	U	A	U	SS
<i>Rhinoceros sondaicus</i>	MNHN	ZM-AC-A7971	U	A	W	SS
<i>Rhinoceros sondaicus</i>	NHMUK	ZD 1861.3.11.1	U	S	W	SS
<i>Rhinoceros sondaicus</i>	NHMUK	ZD 1871.12.29.7	M	A	W	SS
<i>Rhinoceros sondaicus</i>	NHMUK	ZD 1921.5.15.1	F	S	W	SS
<i>Rhinoceros sondaicus</i>	RBINS	1205F	U	S	W	SS
<i>Rhinoceros unicornis</i>	AMNH	M-35759	M	A	C	SS
<i>Rhinoceros unicornis</i>	AMNH	M-54456	F	A	W	SS
<i>Rhinoceros unicornis</i>	MNHN	ZM-AC-1960-59	M	A	C	SS

(Continues)

TABLE 1 (Continued)

Taxon	Institution	Specimen number	Sex	Age	Condition	3D acquisition
<i>Rhinoceros unicornis</i>	NHMUK	ZD 1884.1.22.1.2	F	A	W	SS
<i>Rhinoceros unicornis</i>	NHMUK	ZE 1950.10.18.5	M	A	W	SS
<i>Rhinoceros unicornis</i>	NHMUK	ZE 1961.5.10.1	M	A	W	SS
<i>Rhinoceros unicornis</i>	NHMUK	ZD 1972.822	U	A	U	SS
<i>Rhinoceros unicornis</i>	RBINS	1208	F	A	C	SS
<i>Rhinoceros unicornis</i>	RBINS	33382	U	A	U	SS

Age: A, adult; C, captive; M, male; P, photogrammetry. Sex: F, female; S, sub-adult. Condition: W, wild; U, unknown. 3D acquisition: SS, surface scanner; U, unknown. Institutional abbreviations: AMNH, American Museum of Natural History, New York; BICPC, Powell Cotton Museum, Birchington-on-Sea; CCEC, Centre de Conservation et d'Étude des Collections, Musée des Confluences, Lyon; MNHN, Muséum National d'Histoire Naturelle, Paris; NHMUK, Natural History Museum, London; NHMW, Naturhistorisches Museum Wien, Vienna; RBINS, Royal Belgian Institute of Natural Sciences, Brussels; RMCA, Royal Museum for Central Africa, Tervuren; ZSM, Zoologische Staatssammlung München, Munich. Specimens MNHN-ZM-AC-1885-734, NHMUK ZD 2018.143 and NHMUK ZD 1972.822 were previously determined or reattributed based on the analysis of the limb long bone morphology (see Mallet *et al.*, 2019).

used the same number and position for anatomical landmarks and curve sliding semi-landmarks as in the protocol described in Mallet *et al.* (2019) but the number of surface sliding semi-landmarks was reduced for all the bones—except the fibula—to improve the computation duration (see Supporting Information Data S2). The specimen C. *simum* RMCA 1985.32-M-0001 was arbitrarily chosen as the initial specimen on which all anatomical landmarks, curve and surface sliding semi-landmarks were placed. This specimen was then used as a template for the projection of surface sliding semi-landmarks on the surface of all other specimens. Projection was followed by a relaxation step to ensure that projected points matched the actual surface of the meshes. Curve and surface sliding semi-landmarks were then slid to minimize the bending energy of a thin plate spline (TPS) between each specimen and the template first, and then four times between the result of the previous step and the Procrustes consensus of the complete dataset. Therefore, all landmarks can be treated at the end as geometrically homologous (Gunz, Mitteroecker & Bookstein, 2005). After the sliding step, we performed a Generalized Procrustes Analysis (GPA) to remove the effect of size, location and orientation of the different landmark conformations (Gower, 1975; Rohlf and Slice, 1990). Projection, relaxation, sliding processes and GPA were conducted using the 'Morpho' package (v2.7) in the R environment (v3.5.1—R Core Team, 2014). Details of the process are provided in the documentation of the package (Schlager, 2017).

## 2.4 | Study of morphological integration

We explored 15 covariation patterns among all the possible pairs of bones (Gasc, 2001; Schmidt and Fischer, 2009): within-limbs adjacent bones (humerus-radius, humerus-ulna, radius-ulna, femur-tibia, femur-fibula and tibia-fibula), serially homologous bones (humerus-femur, radius-tibia, radius-fibula, ulna-tibia and ulna-fibula) and functionally analogous bones (humerus-tibia, humerus-fibula) (Figure 1). If the serial homology for the stylopodial bones seems obvious, no clear consensus exists for the serial homology within

the zeugopodium elements. Many studies consider the radius and the tibia, and the ulna and the fibula, as serially homologous, respectively (Bininda-Emonds *et al.*, 2007; Schmidt and Fischer, 2009; Martín-Serra *et al.*, 2015; Hanot *et al.*, 2017; Botton-Divet *et al.*, 2018), unfortunately without strong developmental or genetic evidences. Recent studies tend to indicate that the apparently obvious homology between fore- and hind limb segments might be much more spurious than previously thought (Diogo and Molnar, 2014; Sears *et al.*, 2015). In this context, we therefore tested the four possible bone combinations in the zeugopodium. As the appendicular skeleton is known to be highly integrated among quadrupedal mammals (Schmidt and Fischer, 2009; Martín-Serra *et al.*, 2015; Hanot *et al.*, 2017; Botton-Divet *et al.*, 2018), we also tested the combinations involving non-homologous or analogous bones (radius-femur and ulna-femur) (Figure 1). Covariation patterns were investigated using Two-Blocks Partial Least Squares (2BPLS) analyses. The 2BPLS method extracts the principal axes of covariation from a covariance matrix computed on two shape datasets (Rohlf and Corti, 2000; Botton-Divet *et al.*, 2018; Hanot *et al.*, 2018), allowing the specimen repartition to be visualized relative to these axes and the shape changes associated.

Each PLS axis is characterized notably by its explained percentage of the overall covariation, its PLS correlation coefficient (rPLS) and its *p*-value, computed as a singular warp analysis as detailed in Bookstein *et al.* (2003). The *p*-value was considered significant when the observed rPLS was higher than the ones obtained from randomly permuted blocks (1,000 permutations). When the *p*-value was below .05, the PLS was considered significant, i.e. the two considered blocks were considered significantly integrated. We used the function 'pls2b' in the 'Morpho' package to compute the 2BPLS (Schlager, 2017). To visualize these shape changes along the PLS axes, we used the function 'plsCoVar' in the 'Morpho' package to compute theoretical shapes at two standard deviations on each side of each axis (see Schlager, 2017). These theoretical conformations were then used to calculate a TPS deformation of the template mesh and therefore visualize the shape changes along the PLS axes. We

**FIGURE 2** Plots of the first PLS axes computed on raw shapes. a: humerus-radius; b: humerus-ulna; c: humerus-femur; d: humerus-tibia; e: humerus-fibula; f: radius-ulna; g: radius-femur. rPLS: value of the PLS coefficient; % EC: percentage of explained covariation; Corr. *p*-value: corrected *p*-value using a Benjamini-Hochberg correction. The phylogenetic tree displays a polytomy because of the absence of consensus regarding the relationships of the five modern rhinos

then used the function 'meshDist' in the 'Morpho' package to create colour maps indicating the location and the intensity of the covariation between two meshes by mapping the distance between the minimum and maximum theoretical shapes along the first PLS axis (areas in red are the ones showing the most shape changes within a bone pair, whereas the areas in blue are the ones showing fewer shape changes).

This procedure was performed at an interspecific level including all the 50 specimens into a single GPA. We also explored the intraspecific level of covariation by performing the sliding and GPA procedures on subsamples containing each different species. We then obtained five specific datasets on which to perform 2BPLS analyses.

## 2.5 | Effect of allometry

It has been previously demonstrated that centroid size may be a good approximation of the body mass of the specimen (Ercoli and Prevosti, 2011; Cassini *et al.*, 2012), notably among modern rhinos (Mallet *et al.*, 2019). To assess the effect of body mass on integration patterns, i.e. the effect of evolutionary allometry, we computed a multivariate regression of the shape against the centroid size using the function 'procD.lm' in the 'geomorph' package (v3.1.2—Adams and Otárola-Castillo, 2013). The residuals were then used to compute allometry-free shapes, which were analysed with 2BPLS as described previously. Each species may have its own allometric slope, making it difficult to remove the general allometry effect (Klingenberg, 2016). However, considering previous results on rhino long bones that indicated close allometric slopes for the different species (Mallet *et al.*, 2019) and the reduced sample size inherent to studying this endangered group, we chose to provide allometry-free shapes using a single allometric component among all species (evolutionary allometry).

## 2.6 | Statistical corrections for multiple comparisons

As explained above, we performed multiple pairwise comparisons when computing the different PLS. Each analysis tested a different pair of bones and contained part of the data present in some other analyses (e.g. landmarks of the humerus are tested for covariation with those of the radius, but also in all other pairs involving the humerus). For each tested pair, the hypothesis was that there was a significant covariation between the shapes of the two bones. Given these settings and the exploratory approach of the study, there is no common agreement in the literature regarding whether statistical corrections for multiple comparisons should be used in the present case to lower the risk of finding false positives (i.e. finding a

significant result due to chance) (Cabin and Mitchell, 2000; Streiner and Norman, 2011). In this context, we chose to present and discuss both uncorrected and corrected analyses for multiple comparisons, especially for the analyses at the intraspecific level, where the correction had a higher impact (see Results). We applied a Benjamini-Hochberg correction to our data (Benjamini and Hochberg, 1995) as described by Randau and Goswami (2018) in a similar context of covariation tests on 3D geometric morphometric data. The test was run in R using the function 'p.adjust' in the 'stats' package. This correction was applied to all our tests at the interspecific and intraspecific levels.

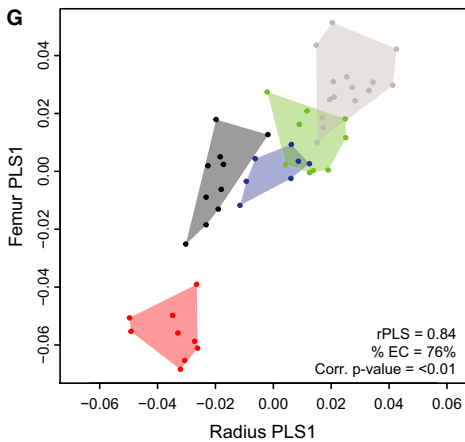
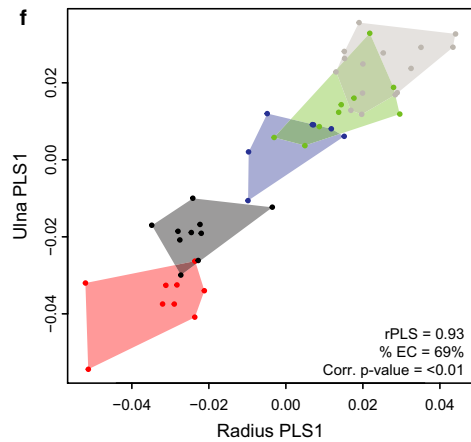
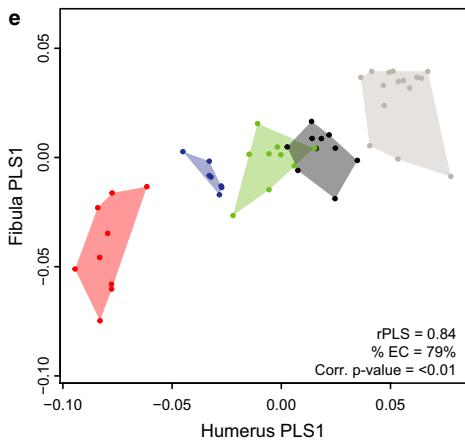
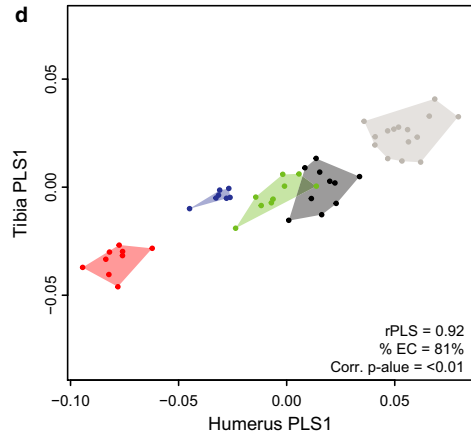
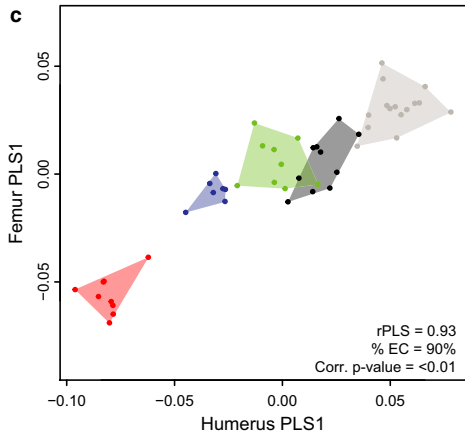
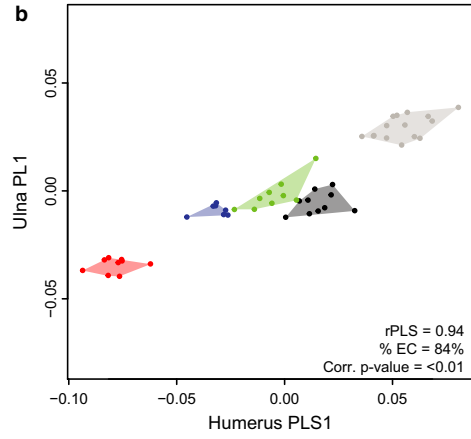
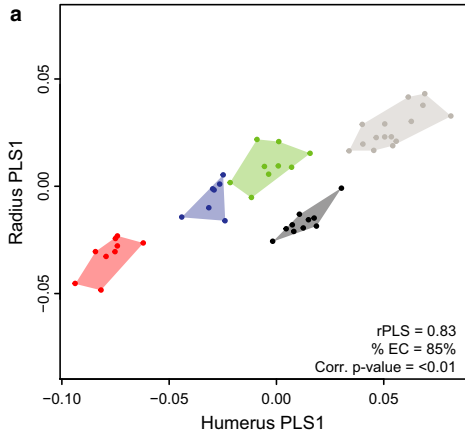
## 3 | RESULTS

### 3.1 | Covariation at the interspecific level

All the first PLS axes are highly significant (*p*-values < .01 after correction – see Figures 2 and 3). These first axes make up between 53% (tibia-fibula) and 90% (humerus-femur) of the total covariation. Similarly, the rPLS values are high and vary between 0.72 (tibia-fibula) and 0.94 (humerus-ulna), indicating a strong general integration of the limb bones (Figure 4a). Intra-limb bones covary slightly more strongly in the forelimb than in the hind limb (Figure 4a). Surprisingly, the humerus and the ulna covary slightly more (rPLS = 0.94) compared with the radius-ulna pair (rPLS = 0.93). In the hind limb, despite a high degree of covariation between the femur and the tibia (rPLS = 0.89), these two bones are poorly integrated with the fibula. When looking at serially homologous bones, the integration appears stronger between the humerus and the femur (rPLS = 0.93) and the ulna and the tibia (rPLS = 0.92) than between the radius and the tibia (rPLS = 0.88) and the ulna and the fibula (rPLS = 0.82). The radius-fibula covariation is the weakest (rPLS = 0.76) of all serially homologous bones. Regarding the functionally analogous bones, the covariation between the humerus and the hind limb zeugopodial bones is strong and more marked with the tibia (rPLS = 0.92) than with the fibula (rPLS = 0.84). Finally, the non-homologous or functionally analogous bones also reveal a stronger covariation between the ulna and the femur (rPLS = 0.90) than between the radius and the femur (rPLS = 0.84). In summary, all categories of pairwise comparisons (intra-limb, serial homology, functional analogy, non-homologous or analogous bones) showed high but unequal degrees of covariation. The fibula particularly stands out as having relatively weak degrees of covariations with other bones, being the only one not showing at least one very high covariation with another bone.

All plots of the first PLS axes are structured by an opposition between *Ds. sumatrensis* on the negative side and *C. simum* on the positive side (Figures 2 and 3), except for the tibia-fibula pair. *Diceros*





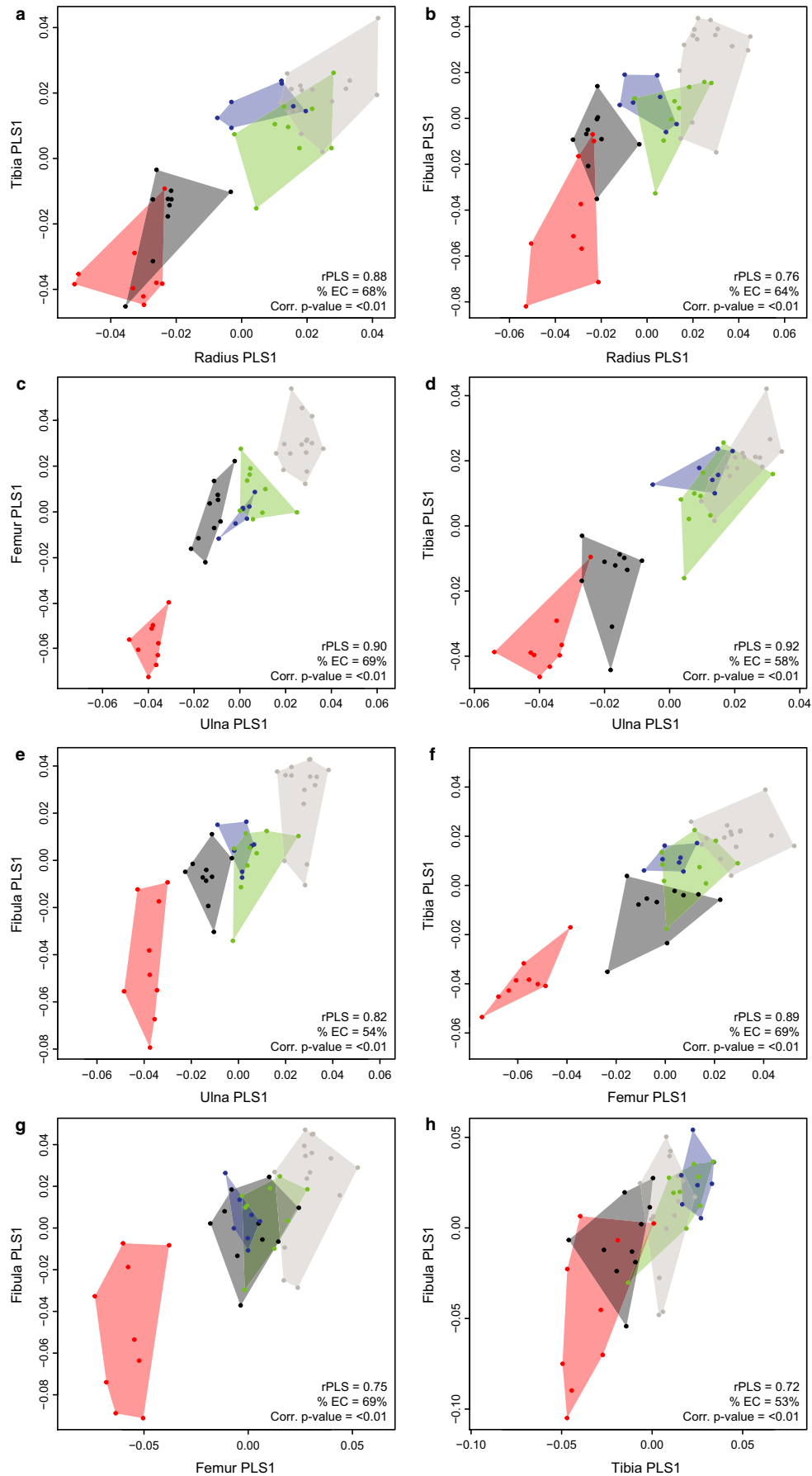


**FIGURE 3** Plots of the first PLS axes computed on raw shapes. a: radius-tibia; b: radius-fibula; c: ulna-femur; d: ulna-tibia; e: ulna-fibula; f: femur-tibia; g: femur-fibula; h: tibia-fibula. rPLS: value of the PLS coefficient; % EC: percentage of explained covariation; Corr. p-value: corrected p-value using a Benjamini-Hochberg correction. Colour code as in Figure 2



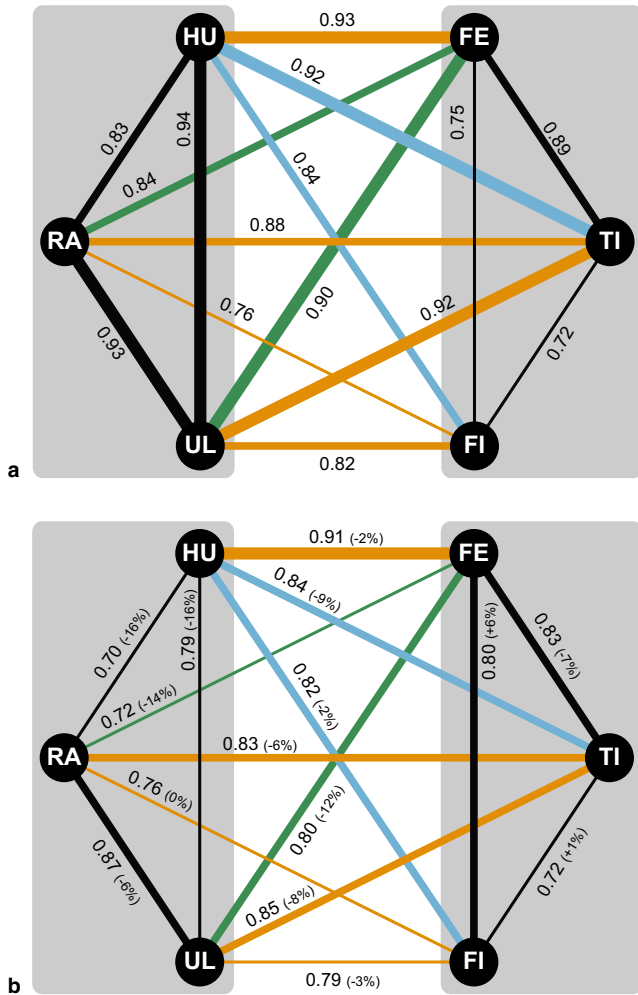


**FIGURE 4** Graphic model of the rPLS values of the first PLS axes computed on the appendicular skeleton of the five modern rhino species. The line thickness is proportional to the rPLS value. The colour code expresses the type of relation between bones as described in the Figure 1. a: rPLS values obtained on raw shapes. b: rPLS values obtained on allometry-free shapes. In brackets are indicated the percentages of difference between rPLS obtained on raw shapes and allometry-free shapes. Hu: humerus; Ra: radius; Ul: ulna; Fe: femur; Ti: tibia; Fi: fibula

*bicornis*, *R. sondaicus* and *R. unicornis* generally plot between these two extremes. All PLS plots involving the humerus display a clear isolation of these three taxa around null values and poorly dispersed clusters (Figure 2a-e). The clusters along the first PLS axis appear structured by a distinction between Asiatic and African taxa (less marked for the humerus-radius [Figure 2a] and the humerus-ulna [Figure 2e] couples), which can reflect an effect of the phylogeny (if considering African and Asiatic groups as sister taxa). This separation between African and Asiatic taxa follows the distribution of body mass within those groups, the lightest species showing the most negative values and the heaviest ones the most positive ones within both geographical groups. For all the bone pairs not involving the humerus, specimens within each species are more widely distributed in the morphospace and are organized differently along the first PLS axis. The radius-ulna first axis clearly expresses a sorting of the species from the lightest

(*Ds. sumatrensis*) on the negative side to the heaviest (*C. simum*) on the positive side (Figure 2f) independently of the phylogenetic affinities between species. Although less clear, this structure also occurs for the radius-femur, radius-fibula, ulna-femur, ulna-fibula and femur-tibia pairs (Figures 2g and 3b,c,e,f). *Dicerorhinus sumatrensis* is strongly isolated on the negative side on all pairs involving the femur (Figures 2c,g and 3c,f,g). A third pattern isolating *Ds. sumatrensis* and *Dc. bicornis* on the negative part from the three other species on the positive part can be observed for the radius-tibia and ulna-tibia pairs (Figure 3a,d). The only first PLS axis showing a clearly different pattern is that of the tibia-fibula pair, where *R. sondaicus* is the most extreme species on the positive part, and *C. simum* and *R. unicornis* clusters overlap (Figure 3h).

The second PLS axes are significant in most cases, except for the humerus-radius and humerus-femur pairs ( $p$ -values > .05 – see Figure S3). These second axes explain between 4% (humerus-femur) and 31% (ulna-tibia) of the global covariation. Most of the PLS plots indicate a separation between the genus *Rhinoceros* and the three other rhino species, with an important overlapping of the clusters in many cases (Figure S3). This distinction is however absent for most of the plots involving the fibula, where the genus *Rhinoceros* may overlap the *Diceros* or *Dicerorhinus* clusters. No clear intraspecific pattern linked to age or sex has been found along these second PLS axes.

Colour maps computed using the theoretical shapes (Figure S4) indicate that covariation associated to the first PLS axes are very similar for each bone regardless of the considered pair. Eight pairs representing the four types of relationship existing between bones are presented in Figures 5 and 6. All other pairs are available in Figure S5. The shape changes are mainly related to an increase of the bone robustness from negative to positive values of the axes, associated to a development of most of the muscular insertions (tubercles and trochanters) and of articular surfaces. For the humerus, most of the shape covariation with the other bones is located on muscular insertion areas, such as the lesser tubercle, the deltoid tuberosity, the lesser tubercle convexity and the epicondylar crest, where the *m. supraspinatus*, the *m. deltoideus*, the *m. subscapularis* and the *m. extensor carpi radialis* insert, respectively (Figure 5a,d). The intensity of the covariation of the deltoid tuberosity is higher with the radius than with all other bones. For the radius, the strongest shape covariation with the other bones is located on the lateral insertion relief where the *m. extensor digitorum communis* inserts on the medial part of the distal epiphysis and, to a lesser extent, on the radial tuberosity, where the *m. biceps brachii* inserts (Figures 5b and 6a). On the medial part of the distal epiphysis, the shape covariation is less intense in the humerus-radius and radius-fibula couples than in the other bone pairs. For the ulna, the shape covariation with the other bones is mainly located on the medial and lateral tuberosities of the olecranon (where the medial and lateral heads of the *m. triceps brachii* insert, respectively) and along the lateral and palmar edges of the shaft, where most of the digit extensors insert (Figures 5c and 6a,d). The shape covariation is slightly more pronounced on the olecranon tuberosity in the radius-ulna pair than in the other pairs. The femur is the bone showing the most similar patterns of shape covariation regardless of the bone pair. The strongest shape covariation with all other bones is located on the third tubercle

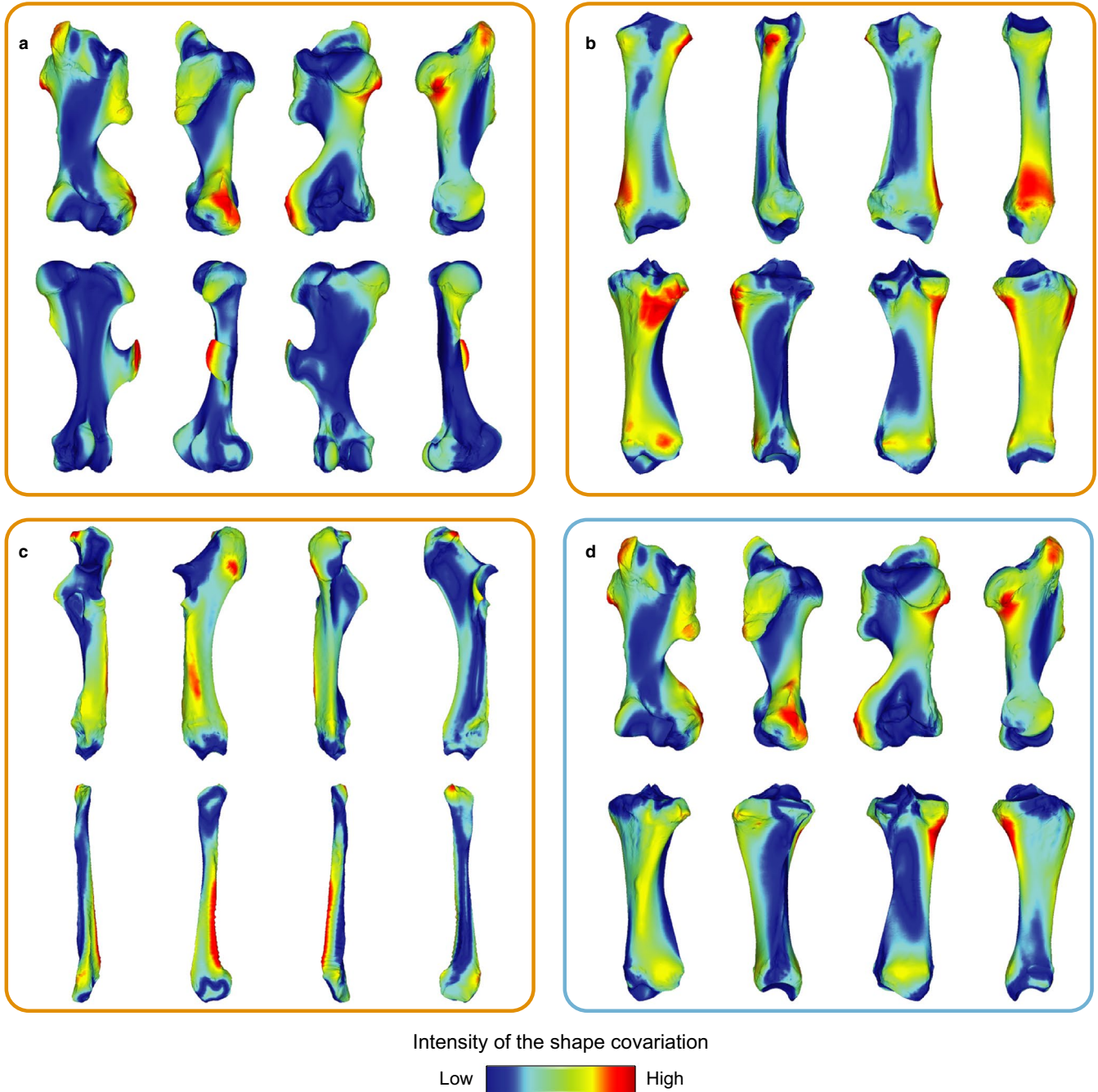


**FIGURE 5** Colour maps of the location and intensity of the shape deformation associated to the first PLS axes for 4 pairs of bones among the five modern species of rhinoceros. For each bone, the shape associated to the positive part of the first PLS axis was coloured depending on its distance to the shape associated to the negative part (blue indicates a low deformation intensity and red indicates a high deformation intensity). The colour code of the squares expresses the type of relation between bones as described in the Figure 1 (orange: serial homology; blue: functional analogy). a: humerus-femur; b: radius-tibia; c: ulna-fibula; d: humerus-tibia (orientation from left to right in each case: cranial, lateral, caudal and medial)

and corresponds to the insertion of the *m. gluteus superficialis*. Other strong shape covariations between the femur and the other bones are located on the greater trochanter convexity, where the *m. gluteus accessorius* inserts, and from the *fovea capitis* to the lesser tubercle, where both the *mm. psoas major* and *iliacus* insert as well as the joint capsule of the hip (Figures 5a and 6b,d). Unlike the femur, the patterns of shape covariation for the tibia are highly variable depending

of the considered bone pair. For the radius-tibia and the ulna-tibia pairs, the strongest shape covariation is mainly located on the tibial tuberosity (where notably the medial, intermediate and lateral patellar ligaments, the patellar fascia and the *fascia lata* insert), the tibial crest, the area located distal to the medial condyle of the tibia, where the *m. popliteus* inserts, and on the cranial and caudal sides of the distal part of the shaft (Figure 5b). The shape covariation is located in the

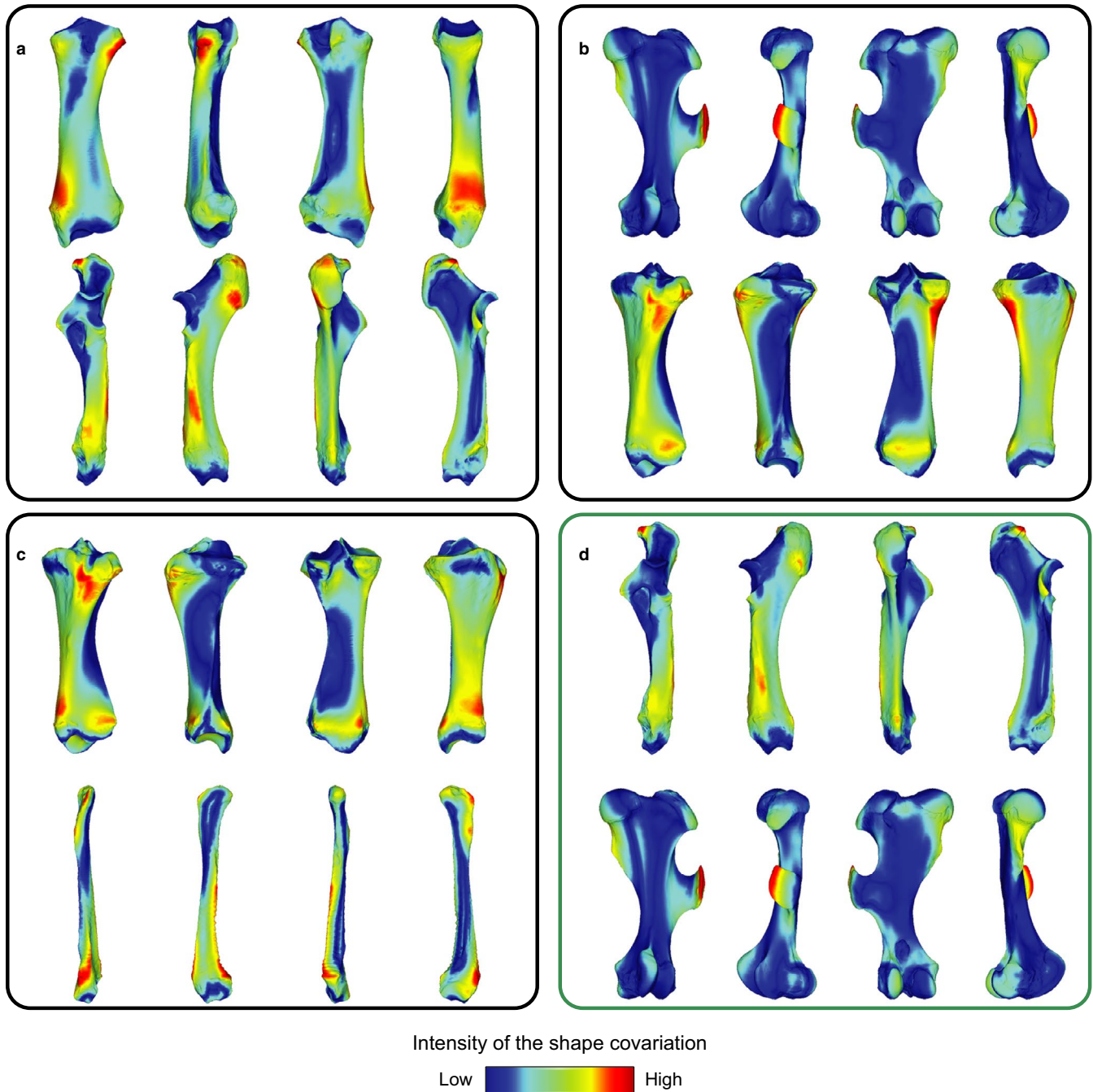


**FIGURE 6** Colour maps of the location and intensity of the shape deformation associated to the first PLS axes for 4 pairs of bones among the five modern species of rhinoceros. For each bone, the shape associated to the positive part of the first PLS axis was coloured depending on its distance to the shape associated to the negative part (blue indicates a low deformation intensity and red indicate a high deformation intensity). The colour code of the squares expresses the type of relation between bones as described in the Figure 1 (black: intra-limb relation; green: non-homologous or analogous bones). a: radius-ulna; b: femur-tibia; c: tibia-fibula; d: ulna-femur (orientation from left to right in each case: cranial, lateral, caudal and medial)

same areas but with less intensity for the femur-tibia and tibia-fibula pairs (Figure 6b,c). The intensity of the shape covariation is minimal for the humerus-tibia pair, except for the insertion of the *m. popliteus* (Figure 5d). Finally, for the fibula, the shape covariation with the other bones is mainly located on the cranial part of the head of the fibula, on the distal part of the cranial crest and on the caudal crest along the shaft, where notably the digit extensors insert (Figures 5c and 6c).

### 3.2 | Allometry-free covariation

All the first PLS axes computed on allometry-free shapes are highly significant ( $p$ -values after correction  $< .01$  – see Figures 7 and 8). The first PLS axes explain between 44% (ulna-fibula) and 87% (humerus-femur) of the total covariation. The rPLS values remain high and range between 0.70 (humerus-radius) and 0.91 (humerus-femur). The rPLS

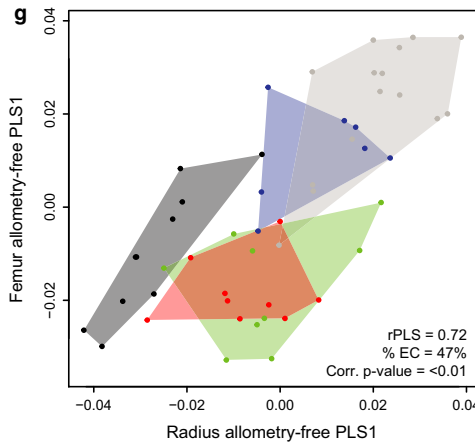
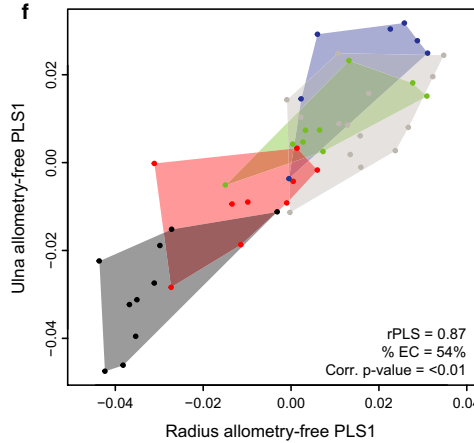
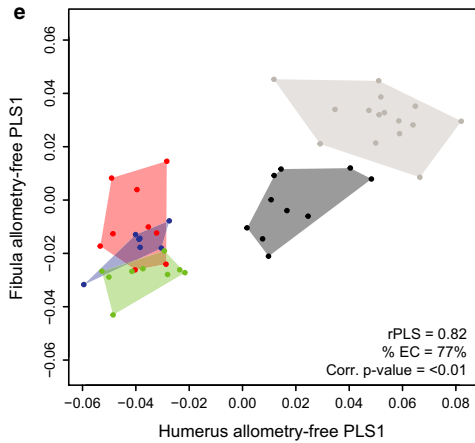
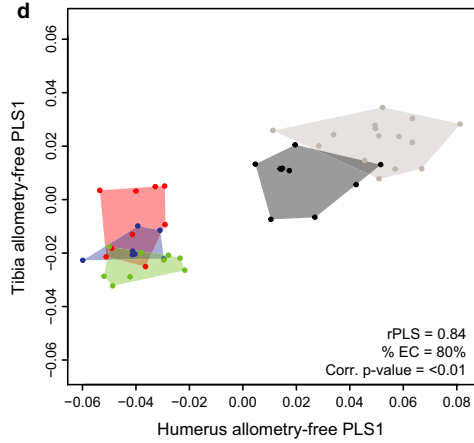
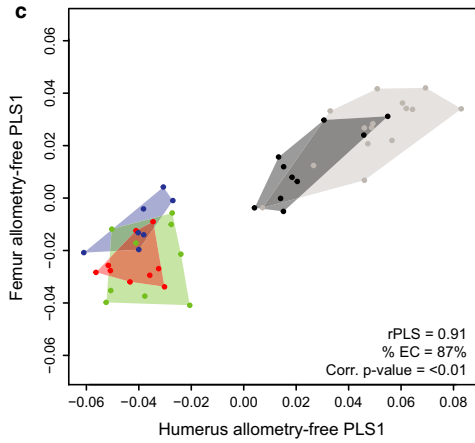
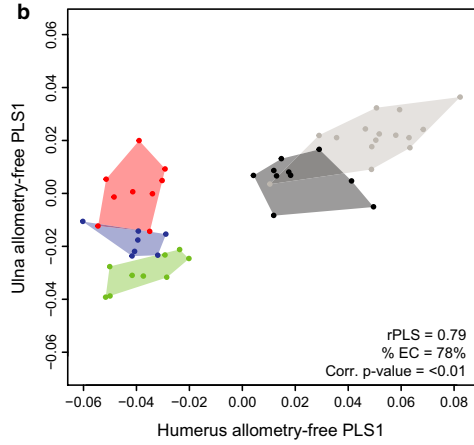
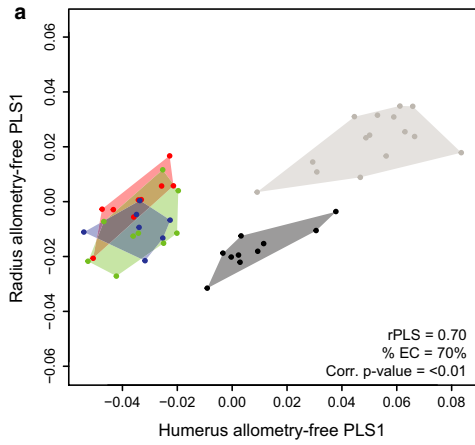




**FIGURE 7** Plots of the first PLS axes computed on allometry-free shapes. a: humerus-radius; b: humerus-ulna; c: humerus-femur; d: humerus-tibia; e: humerus-fibula; f: radius-ulna; g: radius-femur. rPLS: value of the PLS coefficient; % EC: percentage of explained covariation; Corr.  $p$ -value: corrected  $p$ -value using a Benjamini-Hochberg correction. The phylogenetic tree displays a polytomy because of the absence of consensus regarding the relationships of the five modern rhinos

values are unequally impacted by the correction for allometry depending on the considered bone pair. A drop of 12–16% of the rPLS values can be observed between raw and allometry-free shapes for some couples: two intra-limbs pairs (humerus-radius, humerus-ulna) and two non-homologous or functionally analogous bones (radius-femur and ulna-femur) (Figure 4b). The drop of the rPLS values is less marked for other pairs and almost non-existent in the humerus-femur, humerus-fibula and ulna-fibula couples. Moreover, the rPLS value is the same for the radius-fibula pair. We also noticed a slight rise of the rPLS value for the femur-fibula and tibia-fibula pairs of 6 and 1%, respectively.

However, the distribution of the different species and specimens along the first PLS axes is different from the previous analyses (Figures 2 and 3) when computed on allometry-free shapes (Figures 7 and 8). All plots involving the humerus are structured in the same way, with a strong separation between the three Asiatic species on the negative side and the two African species on the positive side (Figure 7a–e). A relatively similar structure is observed for the ulna-femur plot (Figure 8c) but the patterning of the distribution for all other bone pairs distributions is far less clear. Plots for the radius-ulna and the radius-tibia pairs display a similar pattern, with *Dc. bicornis* and *Ds. sumatrensis* grouped together on the negative side, and the three other species on the positive side (Figures 7f and 8a) despite some overlapping. Other plots display various patterns not distinguishing the species based on size, geography or phylogenetic relationships. We can notably see opposite values in *R. unicornis* and *C. simum* at the positive and negative parts of the first axis, respectively, with *Ds. sumatrensis* and *Dc. bicornis* overlapping around null values for the ulna-fibula pair (Figure 8e), or a slight distinction between the *Rhinoceros* genus and the other species for the ulna-tibia pair, whereas *Dc. bicornis* and *R. sondaicus* are strictly opposed along the first PLS axis (Figure 8d). A separation between *R. sondaicus* and the other species is also clearly visible for the tibia-fibula pair (Figure 8h). As for the raw data, the allometry-free shape changes along the first PLS axes mainly concern the robustness of the bones, and shape covariation is very similar for all the bones regardless of the considered pair. All allometry-free theoretical shapes are available in Figure S6.

### 3.3 | Intraspecific covariation

#### 3.3.1 | Without Benjamini-Hochberg correction

At the intraspecific level, rPLS values are relatively high but few first PLS axes are statistically significant, even before correction (Table 2). Analyses reveal that the first PLS axis is significant for five bone pairs within *C. simum* (humerus-radius, humerus-ulna,

humerus-femur, radius-femur and ulna-femur) and *R. sondaicus* (humerus-radius, radius-tibia, radius-fibula, humerus-tibia and ulna-femur), three for *R. unicornis* (humerus-ulna, tibia-fibula and ulna-tibia), two for *Ds. sumatrensis* (humerus-femur and humerus-tibia) and only one for *Dc. bicornis* (ulna-tibia). The rPLS values are extremely high (from 0.89 to 0.99) for *R. sondaicus* relative to the other species (0.72–0.94 for *C. simum*, 0.66–0.96 for *Ds. sumatrensis*, 0.76–0.96 for *Dc. bicornis* and 0.79–0.97 for *R. unicornis*). Although the covariation of some pairs may be common to some taxa (e.g. humerus-radius and ulna-femur for *C. simum* and *R. sondaicus*, humerus-tibia for *Ds. sumatrensis* and *R. sondaicus*), each species displays overall a different pattern of covariation. The lack of significance observed may be due to the small number of specimens per species. However, *C. simum* and *R. sondaicus* show the highest percentage of significant results and are respectively represented by 15 and 7 specimens, these two subsamples being not particularly more diverse than the other species (adults and subadults, males and females, wild and captive specimens—see Figure S7). This indicates that the observed tendency is not only related to the sample size but may also carry a biological signal. Moreover, some bone pairs show a  $p$ -value between .05 and .1 associated with a high rPLS value. This is notably the case for the tibia-fibula pair in the two *Rhinoceros* species (Table 2). This tends to indicate that the shape covariation between the fibula and the tibia may be higher for this clade than for other rhino species. In addition, the rPLS values of other pairs involving the fibula are often higher in both species of *Rhinoceros* than in other species in our sample, although their covariation is rarely significant.

For all these pairs, shape covariation involves anatomical areas which are similar within each species but often different between species (Figure S8). However, some anatomical areas appear to show high shape covariation at both the interspecific and intraspecific levels. This is notably the case of the greater tubercle convexity and the deltoid tuberosity of the humerus and the olecranon tuberosity of the ulna. These areas correspond to the insertion of powerful muscles for flexion and extension of the forearm (respectively *m. infraspinatus*, *m. deltoideus* and *m. triceps brachii*).

#### 3.3.2 | After Benjamini-Hochberg correction

After the Benjamini-Hochberg correction of the  $p$ -values, rPLS values remain statistically significant for only four bone pairs, all belonging to *C. simum*, which is the species with the highest number of specimens (Table 2). In this species, the covariation is extremely strong for the humerus-radius (rPLS = 0.92), the humerus-femur (rPLS = 0.93) and the ulna-femur (rPLS = 0.94) pairs, and slightly weaker for the radius-femur pair (rPLS = 0.89). When looking at the first PLS axes for these four bone pairs, it is clear that the subadults

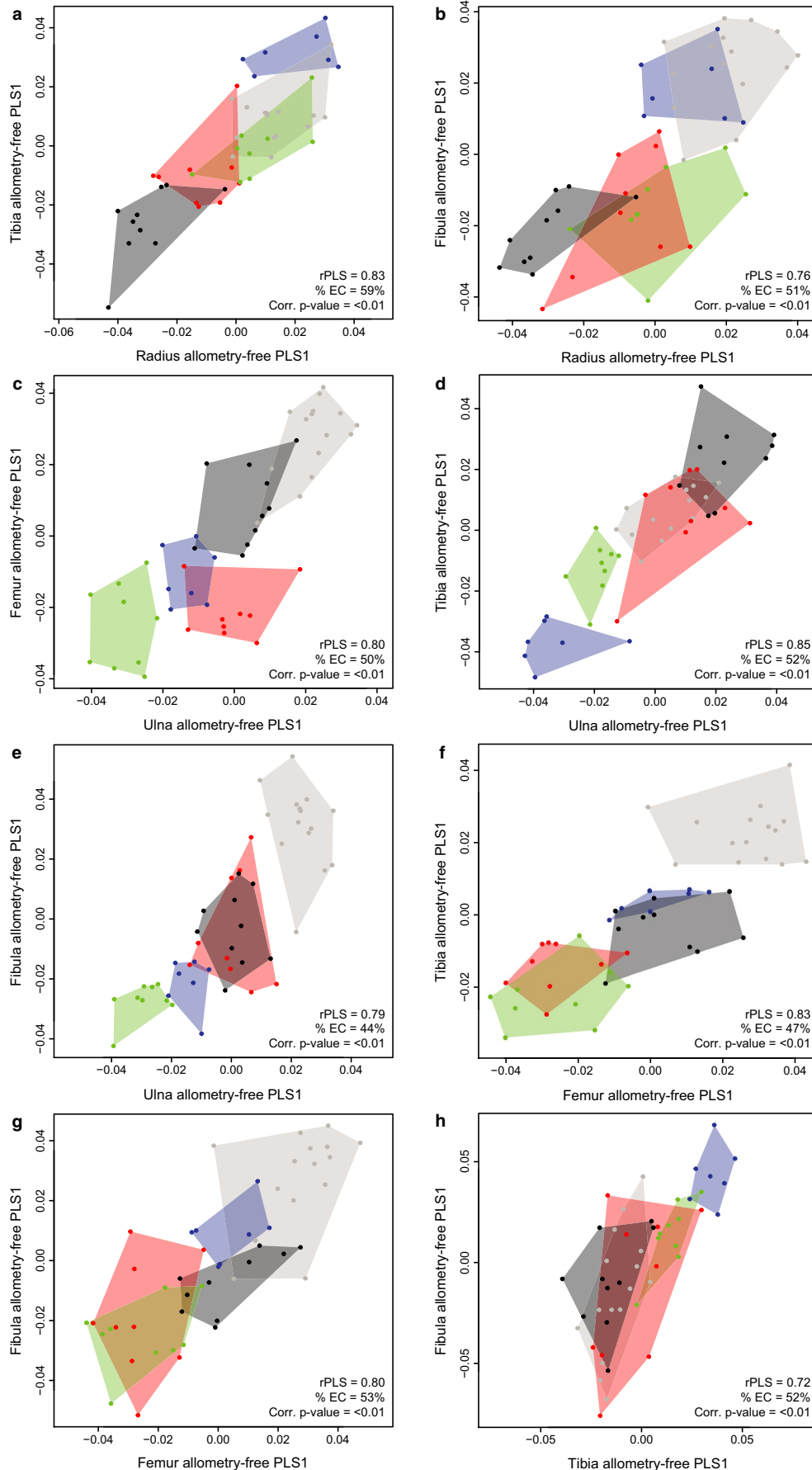


**FIGURE 8** Plots of the first PLS axes computed on allometry-free shapes. a: radius-tibia; b: radius-fibula; c: ulna-femur; d: ulna-tibia; e: ulna-fibula; f: femur-tibia; g: femur-fibula; h: tibia-fibula. rPLS: value of the PLS coefficient; % EC: percentage of explained covariation; Corr. p-value: corrected p-value using a Benjamini-Hochberg correction. Colour code as in Figure 6



**TABLE 2** Values of the rPLS axes for each of the five species, with respective *p*-values before (*p*) and after (*p* cor.) the Benjamini–Hochberg correction

Paired bones	<i>C. simum</i> ( <i>n</i> = 15)			<i>Ds. sumatrensis</i> ( <i>n</i> = 9)			<i>Dc. bicornis</i> ( <i>n</i> = 10)			<i>R. sondaicus</i> ( <i>n</i> = 7)		
	rPLS	<i>p</i>	<i>p</i> cor.	rPLS	<i>p</i>	<i>p</i> cor.	rPLS	<i>p</i>	<i>p</i> cor.	rPLS	<i>p</i>	<i>p</i> cor.
Intra-limb bones												
Hum-Rad	<b>0.92</b>	<b>.01</b>	<b>.04</b>	0.85	.40	.59	0.89	.19	.55	<b>0.98</b>	<b>.01</b>	.10
Hum-Uln	<b>0.91</b>	<b>.04</b>	<b>.11</b>	0.96	.24	.49	0.91	.38	.59	0.98	.17	.23
Rad-Uln	0.88	.07	.16	0.91	.28	.49	0.96	.11	.55	0.97	.09	.15
Fem-Tib	0.85	.25	.36	0.88	.27	.49	0.92	.14	.55	0.97	.09	.15
Fem-Fib	0.78	.87	.87	0.87	.95	.95	0.87	.29	.55	0.95	.26	.30
Tib-Fib	0.72	.12	.26	0.68	.30	.49	0.80	.73	.92	0.98	.08	.15
Serial homology												
Hum-Fem	<b>0.93</b>	<b>.01</b>	<b>.02</b>	<b>0.95</b>	<b>.02</b>	<b>.15</b>	0.91	.59	.80	0.97	.30	.30
Rad-Tib	0.90	.27	.36	0.70	.77	.95	0.94	.23	.55	<b>0.98</b>	<b>.03</b>	.10
Rad-Fib	0.73	.26	.36	0.66	.85	.95	0.76	.81	.55	<b>0.95</b>	<b>.05</b>	.15
Uln-Tib	0.84	.36	.41	0.92	.29	.49	<b>0.94</b>	<b>.05</b>	.55	0.97	.09	.15
Uln-Fib	0.76	.34	.41	0.93	.90	.95	0.89	.99	.99	0.97	.27	.30
Functional equivalence												
Hum-Tib	0.90	.17	.33	<b>0.93</b>	<b>.01</b>	.15	0.86	.21	.55	<b>0.99</b>	<b>.01</b>	.10
Hum-Fib	0.77	.65	.69	0.80	.63	.85	0.90	.81	.93	0.95	.11	.16
Non-homologous or functionally equivalent												
Rad-Fem	<b>0.89</b>	<b>.01</b>	<b>.05</b>	0.89	.07	.33	0.89	.40	.59	0.96	.29	.30
Uln-Fem	<b>0.94</b>	<b>.01</b>	<b>.04</b>	0.93	.19	.49	0.89	.86	.93	<b>0.98</b>	<b>.02</b>	.10

Statistically significant values are presented in bold (*p* or *p* cor. < .05).

Fem, femur; Fib, fibula; Hum, humerus; Rad, radius; Tib, tibia; Uln, ulna.

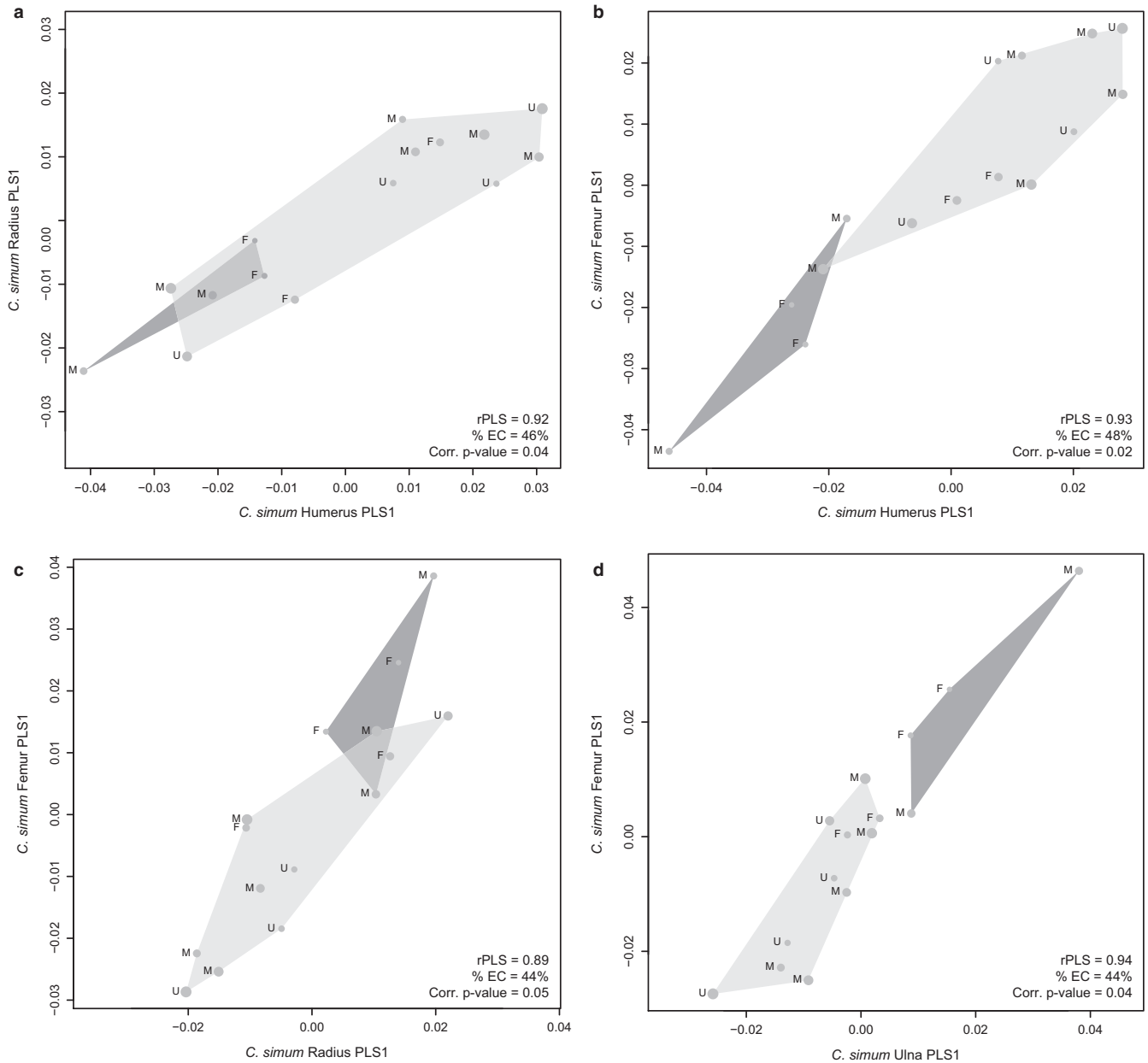


**FIGURE 9** Plots of the first PLS axes computed on the 15 *Ceratotherium simum* specimens. Adults are highlighted in light grey and subadults in dark grey. The size of the dots is proportional to the combined value of the centroid size of the bones for each block and each specimen. a: humerus-radius; b: humerus-femur; c: radius-femur; d: ulna-femur. Sex: F: female; M: male; U: unknown; rPLS: value of the PLS coefficient; % EC: percentage of explained covariation; Corr. *p*-value: corrected *p*-value using a Benjamini-Hochberg correction

are separated from the adults, sometimes without overlap, as for the ulna-femur pair (Figure 9). Contrary to the age class, the size of the individuals (expressed by the sum of the centroid sizes of the two bones in each case) does not seem to follow a precise pattern along the first PLS axes for these four bone pairs (Figure 9). A slight distinction between males and females observed along the first PLS axes may partly account for the sexual dimorphism that exists in this species (Groves, 1972; Guérin, 1980). However, our data are not sufficient for us to conclude a potential difference of integration level due to sexual dimorphism in *C. simum*.

Although not statistically significant before and after correction, similar distinctions between adults and subadults have been

observed on the first PLS axes for *Dc. bicornis* for some bone pairs (mainly humerus-radius, humerus-ulna, humerus-femur, humerus-tibia and radius-femur). Details on age class are too often missing for the three Asiatic species for a conclusion concerning this. Shape variation associated to the first PLS axes in the significant covariations after correction in *C. simum* shows a different tendency than at the interspecific level. The increase in robustness mainly concerns the shaft of the bone, both epiphyses tending to be already very large in subadults. This is particularly the case for the humerus and the femur (Figure 10). Colour maps confirm that the shape covariation along the first PLS axes for *C. simum* concerns different areas than at the interspecific level, with a different intensity depending

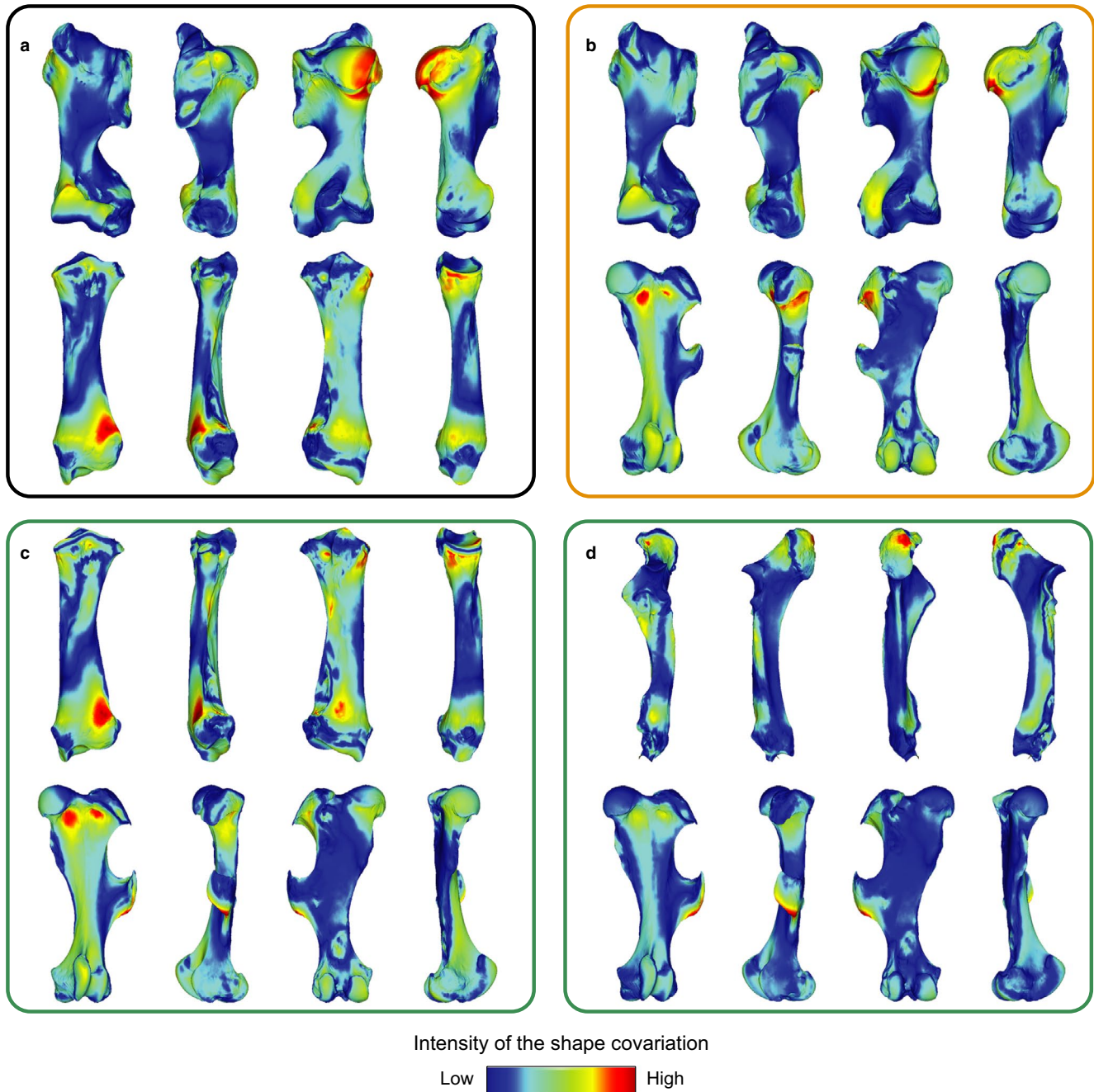


**FIGURE 10** Colour maps of the location and intensity of the shape deformation associated to the first PLS axes for four bones of *Ceratotherium simum*. For each bone, the shape associated to the positive part of the first PLS axis was coloured depending on its distance to the shape associated to the negative part (blue indicates a low deformation intensity and red indicates a high deformation intensity). The colour code of the squares expresses the type of relation between bones as described in the Figure 1 (black: intra-limb relation; orange: serial homology; green: non-homologous or analogous bones). a: humerus-radius; b: humerus-femur; c: radius-femur; d: ulna-femur (orientation from left to right in each case: cranial, lateral, caudal and medial)

on the bone pairs (Figure 10). Notably, we observed that the cranial side of the femur covaries strongly with the humerus and the radius, but visibly less with the ulna (Figure 10b–d). However, some anatomical areas are similarly affected by shape covariation both at the intra- and interspecific levels. This is notably the case for the lesser tubercle tuberosity on the humerus (insertion of the *m. subscapularis*) (Figure 10a,b) and the greater trochanter convexity on the femur (insertion of the *m. gluteus accessorius*) (Figure 10b,c).

## 4 | DISCUSSION

### 4.1 | Patterns of evolutionary integration

Our results indicate that the limb long bones of modern rhino species are strongly integrated at the interspecific level, confirming our first a priori hypothesis. This tendency has been previously observed on limb bones among other terrestrial mammal groups, notably in

equids (Hanot *et al.*, 2017; 2018; 2019), but also in more phylogenetically distant and older clades such as carnivorans (Fabre *et al.*, 2014; Martín-Serra *et al.*, 2015; Botton-Divet *et al.*, 2018) and marsupials (Martín-Serra and Benson, 2019). The high shape covariation between functionally analogous bones (humerus-tibia) as well as between non-analogous bones (ulna-femur) tends to indicate that this strong general integration may be related to a highly coordinated locomotion, as observed in equids at the interspecific level (Hanot *et al.*, 2017), which agrees with the ability of rhinos to gallop (Alexander and Pond, 1992) and to reach high running speed (Blanco *et al.*, 2003).

However, contrary to our second hypothesis, this integration is unequally distributed among the tested pairs of bones. The within-limb integration is slightly stronger in the forelimb than in the hind limb, whereas in other taxa, the morphological integration is generally higher in the hind limb (Martín-Serra *et al.*, 2015; Hanot *et al.*, 2017; Botton-Divet *et al.*, 2018). The covariation is maximal for the humerus-ulna and the radius-ulna couples. Although the femur and the tibia display a strong covariation with one another, the fibula appears as the bone showing the lowest integration level. This is consistent with previous observations on morphological variation of rhino long bones, highlighting the highly variable shape of the fibula at the intraspecific level (Mallet *et al.*, 2019). Therefore, the apparently lower integration of the hind limb may be mainly due to the independent shape variation of the fibula. The fibula nevertheless appears to be more strongly integrated with the humerus (functionally analogous) and the ulna (serially homologous) than with other hind limb bones. This confirms that the shape of the fibula remains covariant with other bones beyond stochastic variation, potentially driving the slightly lower integration of the hind limb than of the forelimb.

## 4.2 | Body mass and evolutionary integration

### 4.2.1 | Within limbs

Among modern rhinos, most of the shape covariation is mainly driven by an increase in general robustness and in the size of the articular surfaces and muscular insertion areas. This agrees with previous observations on other quadrupedal mammals (Martín-Serra *et al.*, 2015; Botton-Divet *et al.*, 2018; Hanot *et al.*, 2018). The correction for allometry affects both the rhino species distribution along the PLS axes and the rPLS values in a stronger way than for equids (Hanot *et al.*, 2018), carnivorans (Martín-Serra *et al.*, 2015) or musteloids (Botton-Divet *et al.*, 2018) at the interspecific level, confirming our third hypothesis that body mass has a stronger influence on the degree of integration among heavy quadrupedal mammal species than in lighter ones. Allometry is also clearly more pronounced on the forelimb than on the hind limb, as shown by the drastic reduction of the integration intensity when using the allometry-free shapes. This would appear to indicate that beyond the strong general integration of the rhino limb bones, the overall higher integration within the forelimb may be caused by a stronger allometry in these

bones—and thus is more strongly affected by body mass (Ercoli and Prevosti, 2011; Cassini *et al.*, 2012; Mallet *et al.*, 2019)—than the hind limb. Heavy quadrupeds bear a larger part of the body weight on their forelimbs than on their hind limbs (Hildebrand, 1974) and rhinos follow this body plan (Regnault *et al.*, 2013) due to their heavy head and horns and their massive trunk muscles and bones. Previous observations (Schmidt and Fischer, 2009; Hanot *et al.*, 2018) led to the conclusion that body mass can contribute to covariation between bones, which our data seem to confirm for rhinos. The higher integration of the forelimb may thus be interpreted as a specialization linked to weight bearing (Martín-Serra *et al.*, 2015; Randau and Goswami, 2018).

Furthermore, the covariation of the different elements composing the forelimb is probably related to a complementary effect of phylogenetic relationships, developmental constraints and body mass. The shape covariation between the humerus and the zeugopodium elements in the forelimb is clearly driven by a distinction between Asiatic and African species, associated with a sorting linked to the mean body mass in these two groups. The covariation is particularly strong between the humerus and the ulna, and although it seems to be largely patterned on phylogenetic history, this is congruent with previous studies indicating a high integration level between the bones involved in flexion/extension movements and body stability (Fabre *et al.*, 2014). Conversely, the interspecific covariation of the radius-ulna pair seems intimately linked to the mean body mass of rhino species, with no distinct link to the phylogenetic pattern. This indicates a likely major impact of mass on the zeugopodium integration, coupled with a common developmental origin (Young and Hallgrímsson, 2005; Sears *et al.*, 2007). These results are also in good agreement with the more important impact of body mass observed on the shape of the radius and ulna than on that of the humerus (Mallet *et al.*, 2019) and the role of the zeugopodium in the support of the bodyweight due to the alignment of this segment with pressure forces (Bertram and Biewener, 1992).

Albeit less obvious, an effect of body mass on the hind limb interspecific integration could also exist, especially between the femur and the tibia when looking at the species distribution along the first PLS axis (raw shapes) and the rPLS values for allometry-free shapes. In a similar way to the forelimb, these two bones are involved in leg flexion/extension, particularly for propulsion (Hildebrand, 1974; Lawler, 2008; Biewener and Patek, 2018). Conversely, the degree of integration increases between the femur and the fibula (and to a lesser extent between the tibia and the fibula) when the allometric effect is removed, which is a unique phenomenon among all tested limb bone pairs. One interpretation could be that the allometry effect consists in antagonistic changes between the femur and the fibula, and that the fibula shape covariation at the interspecific level is poorly related to body mass. This is consistent with all low rPLS drops for allometry-free shapes in all other pairs involving the fibula. This difference can also be influenced by a different covariation between the femur and the fibula depending on the rhino species (see below). The independence of the shape variation of the fibula relative to the tibia also indicates that, contrary to the forelimb

zeugopodium, neither common developmental origin nor functional requirements seem to place a strong constraint on the covariation between the two hind limb zeugopodium bones.

Following the hypotheses of Hallgrímsson *et al.* (2002) and Young and Hallgrímsson (2005) stating that a functionally specialized part covaries less with surrounding elements, the fibula could be interpreted as a highly specialized bone in some rhino species. However, as previously observed for the ulna of musteloids (Botton-Divet *et al.*, 2018), the lower integration of the fibula may be linked to a decrease of the functional constraints exerted on this bone. The fibula supports the insertion of digit flexors and extensors (Barone, 2010) and is involved in ankle stability and weight bearing among rhinos. However, the fibula shape has been proven to be poorly correlated with body mass (Mallet *et al.*, 2019). Therefore, it is likely that the fibula shape varies more independently and is less functionally constrained by body mass than other limb bones in some rhino species (see below). This may be interpreted as a case of parcellation (Young and Hallgrímsson, 2005) due to a functional dissociation between the bones of a single limb.

All the pairs involving the humerus seem thus more strongly impacted by phylogeny than by functional constraints and, to a lesser extent, by body mass. Most of the other bone pairs rather suggest a dominant effect of body mass, especially the ones involving the radius and the ulna. Although less clear, similar results were obtained for the hind limb bones.

#### 4.2.2 | Between limbs

At the interspecific level, serially homologous bones are strongly integrated but their covariation is differently associated with body mass, i.e. more for the zeugopodium elements than for the stylopodium ones. Together with the slightly lower integration values of the zeugopodium elements relative to the stylopodium, these observations are also consistent with previous studies indicating a decrease of the integration from proximal to distal parts of the limbs linked to a higher degree of specialization of distal elements (Young and Hallgrímsson, 2005). In addition, our results are not congruent with the strict serial homology classically considered for the zeugopodium (radius-tibia and ulna-fibula), as they show a stronger covariation between the ulna and the tibia than between the radius and the tibia. Similar results were observed on carnivorans and interpreted as a potential functional convergence between these bones (Martín-Serra *et al.*, 2015). These results could also revive doubts concerning the a priori hypothesis of homology between zeugopodium bones, which has long been debated (Owen, 1848; Wyman, 1867; Lessertisseur and Saban, 1967) and which, to our knowledge, still remains unresolved, although largely taken for granted (i.e. Bininda-Emonds *et al.*, 2007; Bennett and Goswami, 2011; Martín-Serra *et al.*, 2015; Botton-Divet *et al.*, 2018). Only a comprehensive study of the genetic processes leading to the development of forelimb and hind limb zeugopodium could clarify this aspect (Klingenberg, 2014).

The strong integration between the humerus and the tibia (and the fibula to a lesser extent) tends to confirm the functional analogy between the forelimb stylopodium and the hind limb zeugopodium (Gasc, 2001; Schmidt and Fischer, 2009). However, the shape covariation is weaker in the humerus-tibia pair than in other bone pairs involving the tibia (e.g. radius-tibia and ulna-tibia), which tends to indicate that, in the present case, the functional requirements linked to locomotion and body support during resting time may less affect the shape covariation than the developmental constraints, contrary to what has been observed in lighter taxa (Fabre *et al.*, 2014; Hanot *et al.*, 2017; Botton-Divet *et al.*, 2018). Moreover, the high covariation between the ulna and the femur also addresses the classic functional approach, highlighting a strong integration between non-homologous or analogous bones, an observation also recently revealed among marsupials (Martín-Serra and Benson, 2019). Recent work using a network approach on a phylogenetic matrix of characters among modern and fossil rhinos showed that unexpected covariations can exist between cranial, dental and postcranial phenotypic traits in the group (Lord *et al.*, 2019). In particular, the authors observed a frequent co-occurrence of discrete traits between the radius-ulna and the femur among all rhinos, which seems to be consistent with our results indicating a strong covariation between the forelimb zeugopodium and the hind limb stylopodium. As the postcranial body plan appears to have been implemented early in Rhinoceroidea evolutionary history (Lord *et al.*, 2019) and may be less variable than in phylogenetically close taxa such as equids (McHorse *et al.*, 2019), this may imply strong inherited developmental constraints within this group canalizing the shape covariation (Hallgrímsson *et al.*, 2002) even between non-homologous bones. Furthermore, the high integration of non-homologous or analogous bones appears strongly congruent with the variation in body mass, lending further support to the link between heavy weight and high general integration level (Schmidt and Fischer, 2009; Hanot *et al.*, 2017).

#### 4.3 | Covariation at the intraspecific level: developmental integration

Our exploration of integration patterns at the intraspecific level is limited by the low sample size for all species and the non-significance (at  $p > .05$ ) of most of the PLS axes obtained for the different pairs of bones, particularly after the Benjamini-Hochberg correction. Beyond this strict non-significance (which is currently criticized in favour of a more continuous approach of the  $p$ -value—see Ho *et al.*, 2019; Wasserstein *et al.*, 2019), no clear similar pattern of integration seems to emerge between light and heavy rhino species, or between African and Asiatic species. Some species share the same significant or almost significant bone pairs. The covariation between the tibia and the fibula among *Rhinoceros* notably seems relatively strong compared with other species, confirming previous results on individual shape variation (Mallet *et al.*, 2019). This aspect may indicate that the hind limb zeugopodium—and particularly the fibula—is



less variable among the two species of this genus, with less parcelation in this group.

The integration patterns found in *C. simum*, the species with the most specimens, reveal both similarities and divergences with the patterns observed at the interspecific level (i.e. evolutionary integration, see Cheverud, 1996; Klingenberg, 2014). All the significant PLS axes in this species concern forelimb bones and indicate a very strong integration between the humerus, the radius and the ulna, as well as a high shape covariation between the humerus and the femur (serial homology). The strong integration of the forelimb may be partly related to the heavier and longer head of *C. simum* compared with other species (Guérin, 1980) and highlights different patterns of distribution of bodyweight among modern rhinos (P.-O. Antoine, pers. comm.). The shape covariation among *C. simum* specimens reveals a strong effect of age with a clear separation between adults and subadults in all cases. Even if this effect is not visible at the interspecific level, the separation between the two age classes is the main driver of the integration within this species, whereas body mass (approximately expressed through the value of the centroid size) and sex do not seem to play a visible role on the covariation patterns. This tendency is associated with a shape covariation on anatomical areas that often is different from the ones showing a strong covariation at the interspecific level. Only the greater tubercle convexity and the deltoid tuberosity on the humerus, the olecranon tuberosity on the ulna and the greater trochanter convexity on the femur show a high degree of shape covariance at both interspecific and intraspecific levels.

Within *C. simum*, developmental integration is related more to proportions between the different bone parts (e.g. shaft and epiphyses) than to the development of powerful muscular insertions ensuring the stability and the locomotion of the body. In the end, the global integration of the rhino limb long bones results in the superposition and association of the different levels of integration (here, developmental and evolutionary). These integration levels are jointly influenced by shared phylogenetic history, similar developmental origin and constraints due to both locomotion and body mass support (Cheverud, 1996; Hallgrímsson *et al.*, 2009; Klingenberg, 2014). Investigated here among *C. simum*, the static and developmental integration levels remain to be explored with a larger sample for the other rhino species – which remains challenging for these endangered species. Finally, the addition of some of the numerous fossil taxa belonging to the superfamily Rhinoceroidea and displaying convergent increases of body mass will help testing the influence of body mass on integration patterns suggested in the present study (Klingenberg, 2014).

## 5 | CONCLUSION

Our exploration of the integration patterns of the limb long bones among modern rhinos reveals that the appendicular skeleton of these species is strongly integrated, as in other terrestrial quadrupedal mammals. At the interspecific level, the forelimb appears as

more covariant than the hind limb, with a more apparent relation to body mass, which appears stronger than for more lightly built terrestrial mammals. This can be interpreted as a higher degree of specialization of the forelimb in body weight support. Proximal elements appear primarily affected by common developmental constraints whereas the distal parts of the limbs seem rather shaped by functional requirements, which would confirm hypotheses addressed on different mammal groups. The appendicular skeleton of rhinos appears to be a compromise between the functional requirements of a highly coordinated locomotion, the necessity to sustain a high body mass and important inherited developmental processes constraining shape covariation – located mostly on insertion areas for powerful flexor and extensor muscles. In addition, the exploration of the shape covariation at the intraspecific level reveals a prominent effect of the age class in shaping the covariation patterns among *C. simum*. These results are a first step to explore further the functional construction of the appendicular skeleton of modern rhinos and to extend this approach to other heavy modern taxa (such as elephants or hippos). Moreover, the numerous fossil taxa composing the superfamily Rhinoceroidea and showing a broad range of body mass would be a valuable group to extend these results and highlight convergent patterns of shape covariation directly linked to a heavy weight.

## ACKNOWLEDGEMENTS

The authors would like to warmly thank all the curators of the visited institutions for granting us access to the studied specimens: E. Hoeger and S. Ketelsen (American Museum of Natural History, New York, USA), C. West, R. Jennings, M. Cobb (Powell Cotton Museum, Birchington-on-Sea, UK), D. Berthet (Centre de Conservation et d'Étude des Collections, Musée des Confluences, Lyon, France), J. Lesur, A. Verguin (Muséum National d'Histoire Naturelle, Paris, France), R. Portela-Miguez (Natural History Museum, London, UK), F. Zachos, A. Bibl (Naturhistorisches Museum Wien, Vienna, Austria), O. Pauwels, S. Bruaux (Royal Belgian Institute of Natural Sciences, Brussels, Belgium), E. Gilissen (Royal Museum for Central Africa, Tervuren, Belgium) and A. H. van Heteren (Zoologische Staatssammlung München, Munich, Germany). C.M. acknowledges C. Étienne, R. Lefebvre (MNHN, Paris, France) and P. Hanot (Max Planck Institute for the Science of Human History, Jena, Germany) for constructive discussions and advice on R programming, data analyses and interpretations. All authors would like to thank P.-O. Antoine (University of Montpellier, France) and another anonymous reviewer for their comments that helped to improve the quality of the manuscript, as well as A. Graham (King's College London, UK) for editorial work. This work was funded by the European Research Council and is part of the GRAVIBONE project (ERC-2016-STG-715300).

## AUTHOR CONTRIBUTIONS

C.M. designed the study with significant inputs from A.H., R.C. and G.B. C.M. did the data acquisition with inputs from A.H. C.M. performed the analyses with the help of R.C and all authors interpreted the results. C.M. drafted the manuscript. All authors reviewed and



contributed to the final version of the manuscript, read it and approved it.

## DATA AVAILABILITY STATEMENT

The data that support the findings of this study are available from the corresponding author upon reasonable request.

## ORCID

Christophe Mallet  <https://orcid.org/0000-0002-1982-3803>

Guillaume Billet  <https://orcid.org/0000-0002-3200-1548>

Alexandra Houssaye  <https://orcid.org/0000-0001-8789-5545>

Raphaël Cornette  <https://orcid.org/0000-0003-4182-4201>

## REFERENCES

- Adams, D.C. and Otárola-Castillo, E. (2013) geomorph: an R package for the collection and analysis of geometric morphometric shape data. *Methods in Ecology and Evolution*, 4, 393–399. <https://doi.org/10.1111/2041-210X.12035>
- Adams, D.C., Rohlf, F.J. and Slice, D.E. (2004) Geometric morphometrics: Ten years of progress following the 'revolution'. *Italian Journal of Zoology*, 71, 5–16. <https://doi.org/10.1080/11250000409356545>
- Agisoft. (2018) *PhotoScan*. St. Petersburg: Professional Edition, Agisoft.
- Alexander, R.M.C.N. and Pond, C.M. (1992) Locomotion and bone strength of the white rhinoceros, *Ceratotherium simum*. *Journal of Zoology*, 227, 63–69. <https://doi.org/10.1111/j.1469-7998.1992.tb04344.x>
- Antoine, P.-O. (2002) Phylogénie et évolution des Elasmotheriina (Mammalia, Rhinocerotidae). *Mémoires du Muséum National d'Histoire Naturelle (1993)*, 188, 5–350.
- Artec 3D (2018) *Artec Studio Professional*. Luxembourg: Artec 3D.
- Baker, J., Meade, A., Pagel, M. and Venditti, C. (2015) Adaptive evolution toward larger size in mammals. *Proceedings of the National Academy of Sciences of the United States of America*, 112, 5093–5098. <https://doi.org/10.1073/pnas.1419823112>
- Bardua, C., Felice, R.N., Watanabe, A. et al (2019) A Practical guide to sliding and surface semilandmarks in morphometric analyses. *Integrative Organismal Biology*, 1, obz016. <https://doi.org/10.1093/iob/obz016>
- Barone, R. (2010) *Anatomie comparée des mammifères domestiques. Tome 1: Ostéologie 5ème édition*. Paris: Vigot Frères.
- Bell, E., Andres, B. and Goswami, A. (2011) Integration and dissociation of limb elements in flying vertebrates: a comparison of pterosaurs, birds and bats. *Journal of Evolutionary Biology*, 24, 2586–2599. <https://doi.org/10.1111/j.1420-9101.2011.02381.x>
- Benjamini, Y. and Hochberg, Y. (1995) Controlling the false discovery rate: a practical and powerful approach to multiple testing. *Journal of the Royal Statistical Society: Series B (Methodological)*, 57, 289–300. <https://doi.org/10.1111/j.2517-6161.1995.tb02031.x>
- Bennett, C.V. and Goswami, A. (2011) Does developmental strategy drive limb integration in marsupials and monotremes? *Mammalian Biology*, 76, 79–83. <https://doi.org/10.1016/j.mambio.2010.01.004>
- Bertram, J.E.A. and Biewener, A.A. (1992) Allometry and curvature in the long bones of quadrupedal mammals. *Journal of Zoology*, 226, 455–467. <https://doi.org/10.1111/j.1469-7998.1992.tb07492.x>
- Biewener, A.A. (1983) Allometry of quadrupedal locomotion: the scaling of duty factor, bone curvature and limb orientation to body size. *Journal of Experimental Biology*, 105, 147–171.
- Biewener, A.A. (1989a) Mammalian terrestrial locomotion and size. *BioScience*, 39, 776–783. <https://doi.org/10.2307/1311183>
- Biewener, A.A. (1989b) Scaling body support in mammals: limb posture and muscle mechanics. *Science*, 245, 45–48. <https://doi.org/10.1126/science.2740914>
- Biewener, A.A. and Patek, S.N. (2018) *Animal locomotion*, 2nd edition. New York: Oxford University Press.
- Bininda-Emonds, O.R., Jeffery, J.E., Sánchez-Villagra, M.R., Hanken, J., Colbert, M., Pieau, C. et al (2007) Forelimb-hindlimb developmental timing changes across tetrapod phylogeny. *BMC Evolutionary Biology*, 7, 1–7. <https://doi.org/10.1186/1471-2148-7-182>
- Blanco, R.E., Gambini, R. and Fariña, R.A. (2003) Mechanical model for theoretical determination of maximum running speed in mammals. *Journal of Theoretical Biology*, 222, 117–125. [https://doi.org/10.1016/S0022-5193\(03\)00019-5](https://doi.org/10.1016/S0022-5193(03)00019-5)
- Bokma, F., Godinot, M., Maridet, O. et al (2016) Testing for Depéret's rule (body size increase) in mammals using combined extinct and extant data. *Systematic Biology*, 65, 98–108. <https://doi.org/10.1093/sysbio/syv075>
- Bookstein, F.L. (2015) Integration, disintegration, and self-similarity: characterizing the scales of shape variation in landmark data. *Evolutionary Biology*, 42, 395–426. <https://doi.org/10.1007/s11692-015-9317-8>
- Bookstein, F.L., Gunz, P., Mitteroecker, P., Prossinger, H., Schaefer, K. and Seidler, H. (2003) Cranial integration in Homo: singular warps analysis of the mid-sagittal plane in ontogeny and evolution. *Journal of Human Evolution*, 44, 167–187. [https://doi.org/10.1016/S0047-2484\(02\)00201-4](https://doi.org/10.1016/S0047-2484(02)00201-4)
- Botton-Divet, L., Cornette, R., Fabre, A.-C., Herrel, A. and Houssaye, A. (2016) Morphological analysis of long bones in semi-aquatic mustelids and their terrestrial relatives. *Integrative and Comparative Biology*, 56, 1298–1309. <https://doi.org/10.1093/icb/icw124>
- Botton-Divet, L., Houssaye, A., Herrel, A., Fabre, A.-C. and Cornette, R. (2018) Swimmers, diggers, climbers and more, a study of integration across the Mustelids' locomotor apparatus (Carnivora: Mustelidae). *Evolutionary Biology*, 45, 182–195. <https://doi.org/10.1007/s11692-017-9442-7>
- Cabin, R.J. and Mitchell, R.J. (2000) To Bonferroni or not to Bonferroni: when and how are the questions. *Bulletin of the Ecological Society of America*, 81, 246–248.
- Cappellini, E., Welker, F., Pandolfi, L. et al (2019) Early Pleistocene enamel proteome from Dmanisi resolves Stephanorhinus phylogeny. *Nature*, 1–5. <https://doi.org/10.1038/s41586-019-1555-y>
- Cassini, G.H., Vizcaíno, S.F. and Bargo, M.S. (2012) Body mass estimation in Early Miocene native South American ungulates: a predictive equation based on 3D landmarks. *Journal of Zoology*, 287, 53–64. <https://doi.org/10.1111/j.1469-7998.2011.00886.x>
- Cheverud, J.M. (1982) Phenotypic, Genetic, and Environmental Morphological Integration in the Cranium. *Evolution*, 36, 499–516. <https://doi.org/10.1111/j.1558-5646.1982.tb05070.x>
- Cheverud, J.M. (1996) Developmental Integration and the Evolution of Pleiotropy. *Integrative and Comparative Biology*, 36, 44–50. <https://doi.org/10.1093/icb/36.1.44>
- Cignoni, P., Callieri, M., Corsini, M., Dellepiane, M., Ganovelli, F. and Ranzuglia, Gs. (2008) MeshLab: an Open-Source Mesh Processing Tool, The Eurographics Association. Available at: <https://doi.org/10.2312/LocalChapterEvents/ItalChap/ItalianChapConf2008/129-136> [Accessed 18 February 2020].
- Cubo, J. (2004) Pattern and process in constructional morphology. *Evolution & Development*, 6, 131–133. <https://doi.org/10.1111/j.1525-142X.2004.04018.x>
- Depéret, C. (1907) *Les transformations du monde animal*. Paris: Flammarion.
- Dinerstein, E. (2011) Family Rhinocerotidae (Rhinoceroses). In: *Handbook of the Mammals of the World* (Wilson DE, Mittermeier RA), pp. 144–181. Barcelona: Lynx Edicions.
- Diogo, R. and Molnar, J. (2014) Comparative anatomy, evolution, and homologies of tetrapod hindlimb muscles, comparison with forelimb muscles, and deconstruction of the forelimb-hindlimb serial homology hypothesis. *Anatomical Record*, 297, 1047–1075. <https://doi.org/10.1002/ar.22919>

- Eisenmann, V. and Guérin, C. (1984) Morphologie fonctionnelle et environnement chez les périssodactyles. *Geobios*, 17, 69–74. [https://doi.org/10.1016/S0016-6995\(84\)80158-8](https://doi.org/10.1016/S0016-6995(84)80158-8)
- Ercoli, M.D. and Prevosti, F.J. (2011) Estimación de Masa de las Especies de Sparassodonta (Mammalia, Metatheria) de Edad Santacrucense (Mioceno Temprano) a Partir del Tamaño del Centroide de los Elementos Apendiculares: Inferencias Paleoecológicas. *Ameghiniana*, 48, 462–479. [https://doi.org/10.5710/AMGH.v48i4\(347\)](https://doi.org/10.5710/AMGH.v48i4(347))
- Fabre, A.-C., Cornette, R., Peigné, S. and Goswami, A. (2013) Influence of body mass on the shape of forelimb in musteloid carnivorans. *Biological Journal of the Linnean Society*, 110, 91–103. <https://doi.org/10.1111/bij.12103>
- Fabre, A.-C., Goswami, A., Peigné, S. and Cornette, R. (2014) Morphological integration in the forelimb of musteloid carnivorans. *Journal of Anatomy*, 225, 19–30. <https://doi.org/10.1111/joa.12194>
- Fau, M., Cornette, R. and Houssaye, A. (2016) Photogrammetry for 3D digitizing bones of mounted skeletons: Potential and limits. *Comptes Rendus Palevol*, 15, 968–977. <https://doi.org/10.1016/j.crpv.2016.08.003>
- Federative Committee on Anatomical Terminology (1998) *Terminologia Anatomica*. Stuttgart: Georg Thieme Verlag.
- Gasc, J.-P. (2001) Comparative aspects of gait, scaling and mechanics in mammals. *Comparative Biochemistry and Physiology Part A: Molecular & Integrative Physiology*, 131, 121–133. [https://doi.org/10.1016/S1095-6433\(01\)00457-3](https://doi.org/10.1016/S1095-6433(01)00457-3)
- Gaudry, M. (2017) *Molecular phylogenetics of the rhinoceros clade and evolution of UCP1 transcriptional regulatory elements across the mammalian phylogeny*. Master of Science. Winnipeg: University of Manitoba. Available at: <https://mspace.lib.umanitoba.ca/xmlui/handle/1993/32525> [Accessed 15 October 2018]
- Goswami, A. and Polly, P.D. (2010) Methods for studying morphological integration and modularity. *The Paleontological Society Papers*, 16, 213–243. <https://doi.org/10.1017/S1089332600001881>
- Goswami, A., Smaers, J.B., Soligo, C. and Polly, P.D. (2014) The macroevolutionary consequences of phenotypic integration: from development to deep time. *Philosophical Transactions of the Royal Society B: Biological Sciences*, 369, 20130254. <https://doi.org/10.1098/rstb.2013.0254>
- Gould, S.J. (2002) *The Structure of Evolutionary Theory*. Cambridge, MA: Harvard University Press. Available at: [www.jstor.org/stable/j.ctvj5f433](http://www.jstor.org/stable/j.ctvj5f433) [Accessed 22 November 2019].
- Gower, J.C. (1975) Generalized procrustes analysis. *Psychometrika*, 40, 33–51. <https://doi.org/10.1007/BF02291478>
- Groves, C.P. (1972) *Ceratotherium simum*. *Mammalian Species*, 1–6. <https://doi.org/10.2307/3503966>
- Guérin, C. (1980) Les Rhinocéros (Mammalia, Perissodactyla) du Miocène terminal au Pléistocène supérieur en Europe occidentale. Comparaison avec les espèces actuelles. Documents du Laboratoire de Géologie de l'Université de Lyon.
- Gunz, P. and Mitteroecker, P. (2013) Semilandmarks: a method for quantifying curves and surfaces. *Hystrix, the Italian Journal of Mammalogy*, 24, 103–109.
- Gunz, P., Mitteroecker, P., & Bookstein, F. L. (2005). Semilandmarks in three dimensions. In: *Modern Morphometrics in Physical Anthropology* (ed Slice DE) pp. 73–98. Developments in primatology: Progress and prospects. Boston: Springer. [https://doi.org/10.1007/0-387-27614-9\\_3](https://doi.org/10.1007/0-387-27614-9_3)
- Hallgrímsson, B., Jamniczky, H., Young, N.M., Rolian, C., Parsons, T.E., Boughner, J.C. and et al (2009) Deciphering the palimpsest: Studying the relationship between morphological integration and phenotypic covariation. *Evolutionary Biology*, 36, 355–376. <https://doi.org/10.1007/s11692-009-9076-5>
- Hallgrímsson, B., Willmore, K. and Hall, B.K. (2002) Canalization, developmental stability, and morphological integration in primate limbs. *American Journal of Physical Anthropology*, 119, 131–158. <https://doi.org/10.1002/ajpa.10182>
- Hanot, P., Herrel, A., Guintard, C. and Cornette, R. (2017) Morphological integration in the appendicular skeleton of two domestic taxa: the horse and donkey. *Proceedings of the Royal Society B: Biological Sciences*, 284, 20171241. <https://doi.org/10.1098/rspb.2017.1241>
- Hanot, P., Herrel, A., Guintard, C. and Cornette, R. (2018) The impact of artificial selection on morphological integration in the appendicular skeleton of domestic horses. *Journal of Anatomy*, 232, 657–673. <https://doi.org/10.1111/joa.12772>
- Hanot, P., Herrel, A., Guintard, C. and Cornette, R. (2019) Unravelling the hybrid vigor in domestic equids: the effect of hybridization on bone shape variation and covariation. *BMC Evolutionary Biology*, 19, 1–13. <https://doi.org/10.1186/s12862-019-1520-2>
- Hildebrand, M. (1974) *Analysis of vertebrate structure*. New York: John Wiley & Sons.
- Ho, J., Tumkaya, T., Aryal, S., Choi, H. and Claridge-Chang, A. (2019) Moving beyond P values: data analysis with estimation graphics. *Nature Methods*, 16, 565–566. <https://doi.org/10.1038/s41592-019-0470-3>
- Kelly, E.M. and Sears, K.E. (2011) Reduced phenotypic covariation in marsupial limbs and the implications for mammalian evolution. *Biological Journal of the Linnean Society*, 102, 22–36. <https://doi.org/10.1111/j.1095-8312.2010.01561.x>
- Klingenberg, C.P. (2008) Morphological Integration and Developmental Modularity. *Annual Review of Ecology, Evolution, and Systematics*, 39, 115–132. <https://doi.org/10.1146/annurev.ecolsys.37.091305.110054>
- Klingenberg, C.P. (2014) Studying morphological integration and modularity at multiple levels: concepts and analysis. *Philosophical Transactions of the Royal Society B: Biological Sciences*, 369, 20130249. <https://doi.org/10.1098/rstb.2013.0249>
- Klingenberg, C.P. (2016) Size, shape, and form: concepts of allometry in geometric morphometrics. *Development Genes and Evolution*, 226, 113–137. <https://doi.org/10.1007/s00427-016-0539-2>
- Lawler, R.R. (2008) Morphological integration and natural selection in the postcranium of wild verreaux's sifaka (*Propithecus verreauxi verreauxi*). *American Journal of Physical Anthropology*, 136, 204–213. <https://doi.org/10.1002/ajpa.20795>
- Lessertisseur, J. and Saban, R. (1967) Le squelette. Squelette appendiculaire. In: *Traité de Zoologie. Tome XVI, Fascicule 1: Mammifères* (Grassé P-P), pp. 298–1123. Paris.
- Lord, E., Pathmanathan, J.S., Corel, E., Makarenkov, V., Lopez, P., Bouchard, F. et al (2019) Introducing trait networks to elucidate the fluidity of organismal evolution using palaeontological data. *Genome Biol Evol*, 11, 2653–2665. <https://doi.org/10.1093/gbe/evz182>
- Mallet, C., Cornette, R., Billet, G. and Houssaye, A. (2019) Interspecific variation in the limb long bones among modern rhinoceroses—extent and drivers. *PeerJ*, 7, e7647. <https://doi.org/10.7717/peerj.7647>
- Mallison, H. and Wings, O. (2014) Photogrammetry in Paleontology—A practical guide. *Journal of Paleontological Techniques*, 12, 1–31.
- Martín-Serra, A. and Benson, R.B.J. (2019) Developmental constraints do not influence long-term phenotypic evolution of marsupial forelimbs as revealed by interspecific disparity and integration patterns. *The American Naturalist*, 195, 547–560. <https://doi.org/10.1086/707194>
- Martín-Serra, A., Figueirido, B., Pérez-Claros, J.A. and Palmqvist, P. (2015) Patterns of morphological integration in the appendicular skeleton of mammalian carnivores. *Evolution*, 69, 321–340. <https://doi.org/10.1111/evo.12566>
- McHorse, B.K., Biewener, A.A. and Pierce, S.E. (2019) The evolution of a single toe in horses: causes, consequences, and the way forward. *Integrative and Comparative Biology*, 59, 638–655. <https://doi.org/10.1093/icb/icz050>
- Olson, E.C. and Miller, R.L. (1958) *Morphological Integration*. Chicago: University of Chicago Press.
- Owen, R. (1848) *On the archetype and homologies of the vertebrate skeleton*. London: John Van Voorst.
- R Core Team (2014) *R: A language and environment for statistical computing*. Vienna: R Foundation for Statistical Computing.

- Raia, P., Carotenuto, F., Passaro, F., Fulgione, D. and Fortelius, M. (2012) Ecological specialization in fossil mammals explains cope's rule. *The American Naturalist*, 179, 328–337. <https://doi.org/10.1086/664081>
- Randau, M. and Goswami, A. (2018) Shape covariation (or the lack thereof) between vertebrae and other skeletal traits in felids: the whole is not always greater than the sum of parts. *Evolutionary Biology*, 45, 1–15. <https://doi.org/10.1007/s11692-017-9443-6>
- Regnault, S., Hermes, R., Hildebrandt, T., Hutchinson, J. and Weller, R. (2013) Osteopathology in the feet of rhinoceroses: lesion type and distribution. *Journal of Zoo and Wildlife Medicine*, 44, 918–927. <https://doi.org/10.1638/2012-0277R1.1>
- Rohlf, F.J. and Corti, M. (2000) Use of two-block partial least-squares to study covariation in shape. *Systematic Biology*, 49, 740–753. <https://doi.org/10.1080/106351500750049806>
- Rohlf, F.J. and Slice, D. (1990) Extensions of the procrustes method for the optimal superimposition of landmarks. *Systematic Zoology*, 39, 40–59. <https://doi.org/10.2307/2992207>
- Schlager, S. (2017) Chapter 9 - Morpho and Rvcg - Shape Analysis in R: R-Packages for Geometric Morphometrics, Shape Analysis and Surface Manipulations. In Zheng, G., Li, S. and Székely, G. eds. *Statistical shape and deformation analysis*. London: Academic Press, pp. 217–256.
- Schmidt, M. and Fischer, M.S. (2009) Morphological Integration in Mammalian Limb Proportions: Dissociation Between Function and Development. *Evolution*, 63, 749–766. <https://doi.org/10.1111/j.1558-5646.2008.00583.x>
- Sears, K.E., Behringer, R.R., Rasweiler, J.J. IV et al (2007) The evolutionary and developmental basis of parallel reduction in mammalian zeugopod elements. *The American Naturalist*, 169, 105–117. <https://doi.org/10.1086/510259>
- Sears, K.E., Capellini, T.D. and Diogo, R. (2015) On the serial homology of the pectoral and pelvic girdles of tetrapods. *Evolution*, 69, 2543–2555. <https://doi.org/10.1111/evo.12773>
- Streiner, D.L. and Norman, G.R. (2011) Correction for multiple testing: is there a resolution? *Chest*, 140, 16–18. <https://doi.org/10.1378/chest.11-0523>
- Van Valen, L. (1965) The study of morphological integration. *Evolution*, 19, 347–349. <https://doi.org/10.1111/j.1558-5646.1965.tb01725.x>
- Wasserstein, R.L., Schirm, A.L. and Lazar, N.A. (2019) Moving to a world beyond 'p < 0.05'. *The American Statistician*, 73, 1–19. <https://doi.org/10.1080/00031305.2019.1583913>
- Wiley, D.F., Amenta, N., Alcantara, D.A., Ghosh, D., Joo Kil, Y. and Delson, E. et al (2005) Evolutionary morphing. In *Proceedings of IEEE Visualization 2005*. Minneapolis, Minnesota: IEEE.
- Willerslev, E., Gilbert, M.T.P., Binladen, J., Ho, S.Y.W., Campos, P.F., Ratan, A. et al (2009) Analysis of complete mitochondrial genomes from extinct and extant rhinoceroses reveals lack of phylogenetic resolution. *BMC Evolutionary Biology*, 9, 1–11. <https://doi.org/10.1186/1471-2148-9-95>
- Wyman, J. (1867) On symmetry and homology in limbs. *Proceedings of the Boston Society of Natural History* 9, 1–45.
- Young, N.M. and Hallgrímsson, B. (2005) Serial homology and the evolution of mammalian limb covariation structure. *Evolution*, 59, 2691–2704. <https://doi.org/10.1111/j.0014-3820.2005.tb00980.x>
- Young, N.M., Wagner, G.P. and Hallgrímsson, B. (2010) Development and the evolvability of human limbs. *Proceedings of the National Academy of Sciences of the United States of America*, 107, 3400–3405. <https://doi.org/10.1073/pnas.0911856107>
- Zelditch, M.L., Swiderski, D.L., Sheets, H.D. et al (2012) *Geometric morphometrics for biologists: A Primer*, 2nd edition. London: Academic Press.
- Zschokke, S. and Baur, B. (2002) Inbreeding, outbreeding, infant growth, and size dimorphism in captive Indian rhinoceros (*Rhinoceros unicornis*). *Canadian Journal of Zoology*, 80, 2014–2023. <https://doi.org/10.1139/z02-183>

## SUPPORTING INFORMATION

Additional supporting information may be found online in the Supporting Information section.

**How to cite this article:** Mallet C, Billet G, Houssaye A, Cornette R. A first glimpse at the influence of body mass in the morphological integration of the limb long bones: an investigation in modern rhinoceroses. *J. Anat.* 2020;00:1–23. <https://doi.org/10.1111/joa.13232>